



Cite this: *Nanoscale*, 2025, **17**, 6154

## Small-signal capacitance in ferroelectric hafnium zirconium oxide: mechanisms and physical insights†

Revanth Koduru, \*<sup>a</sup> Atanu K. Saha, <sup>a</sup> Martin M. Frank <sup>b</sup> and Sumeet K. Gupta<sup>a</sup>

This study presents a theoretical investigation of the physical mechanisms governing small-signal capacitance in ferroelectrics, focusing on hafnium zirconium oxide ( $\text{Hf}_{0.5}\text{Zr}_{0.5}\text{O}_2$ , HZO). We utilize a time-dependent Ginzburg–Landau formalism-based 2D multi-grain phase-field framework to simulate the capacitance of metal–ferroelectric–insulator–metal (MFIM) capacitors. Our simulation methodology closely mirrors the experimental procedures for measuring ferroelectric small-signal capacitance, and the outcomes replicate the characteristic butterfly capacitance–voltage behavior. Notably, this behavior can be obtained without invoking traps. We delve into the components of the ferroelectric capacitance associated with the dielectric response and polarization switching, discussing the primary mechanisms – domain bulk response and domain wall response – contributing to the butterfly characteristics. We explore their interplay and relative contributions to the capacitance, correlating them to the polarization switching mechanisms and domain configurations. Additionally, we investigate the impact of increasing domain density with ferroelectric thickness scaling, demonstrating an enhancement in the polarization capacitance component, in addition to the dielectric component. Furthermore, we analyze the contributions of the domain bulk and domain wall responses across ferroelectric thicknesses, relating the capacitive memory window (for memory applications) to the capacitance and revealing a non-monotonic dependence of the maximum memory window on the ferroelectric thickness.

Received 9th September 2024,

Accepted 2nd January 2025

DOI: 10.1039/d4nr03700f

rsc.li/nanoscale

## 1 Introduction

Ferroelectric (FE) materials exhibit spontaneous polarization switched by external electric fields exceeding their coercive field. Historically, this hysteretic property has been of great interest for non-volatile memory applications.<sup>1</sup> The recent discovery of ferroelectricity in doped hafnium oxide ( $\text{HfO}_2$ )<sup>2</sup> has revitalized interest in FE devices. The CMOS compatibility of  $\text{HfO}_2$  has led to the development of multiple flavors of FE devices for cutting-edge applications such as memory, computing in-memory (CiM), neuromorphic systems, and steep-slope transistors.<sup>3–7</sup> The scale-free nature of ferroelectricity in  $\text{HfO}_2$ ,<sup>8</sup> along with other appealing attributes,<sup>6,9–11</sup> has positioned FE devices as promising contenders for future electronics.

Another unique aspect of FE materials is their hysteretic, non-linear small-signal capacitance. This capacitive response,

reflected in the butterfly capacitance–voltage ( $C$ – $V$ ) characteristics, has enabled applications in varactors, tunable filters, and oscillators.<sup>12–16</sup> Recently, researchers have leveraged this FE capacitance property to propose non-destructive sensing for CiM applications.<sup>17–19</sup> Given the broad range of applications for the capacitive behavior of ferroelectrics, a deep understanding of the underlying physical mechanisms assumes great importance for appropriate application-driven device optimization.

Historically, researchers have proposed several models to explain the butterfly  $C$ – $V$  characteristics.<sup>16,20–32</sup> Among these, the modified Johnson's model<sup>20</sup> extends the original Johnson's model<sup>16</sup> for paraelectrics to the FE state. This empirical approach shifts the electric field dependence of the dielectric permittivity to center around the coercive field of the FE material. While effective at reproducing the experimental butterfly  $C$ – $V$  characteristics, its empirical nature limits the insights into the physical mechanisms governing the capacitance behavior.

Another class of approaches<sup>23–27</sup> relates the FE  $C$ – $V$  characteristics to the displacement of polarization domain walls (DWs). For instance, Placeres-Jiménez *et al.*<sup>25</sup> extended Kittel<sup>26</sup>'s approach of modeling DWs as rigid bodies moving

<sup>a</sup>Elmore Family School of Electrical and Computer Engineering, Purdue University, West Lafayette, IN, 47907, USA. E-mail: kodurur@purdue.edu

<sup>b</sup>IBM Research, Yorktown Heights, NY 10598, USA

† Electronic supplementary information (ESI) available. See DOI: <https://doi.org/10.1039/d4nr03700f>



under the action of an external electric field. In their work,<sup>25</sup> the authors considered DWs as stretched membranes under external electric fields and studied their vibrational dynamics considering a linear restoration force. Employing this framework and incorporating the dependence of background permittivity on the electric field, the authors derived the equations for the butterfly *C*–*V* curves. However, these models are tailored for small changes in the applied electric field and often rely on the Preisach model or other phenomenological models to capture the large-signal hysteresis of ferroelectrics. As a result, these models are constrained in relating the capacitive behavior to polarization switching, and FE domain configurations.

Recent works by Massarotto *et al.*<sup>29,31</sup> and Segatto *et al.*<sup>30</sup> have addressed the long-standing gap between large-signal (LS) and small-signal (SS) capacitance characteristics of FE. Through experimental and simulation efforts, these studies have related the differences between LS and SS capacitance behavior to irreversible and reversible polarization switching.<sup>32</sup> In their simulation works<sup>30,31</sup> based on Landau–Ginzburg–Devonshire theory, the authors presented contrasting findings concerning the contribution of traps and FE response to the capacitance behavior. They further proposed that domain wall motion might not significantly contribute to the FE capacitance response. However, these conclusions are contingent upon the assumptions of fixed domains and the absence of inter-domain coupling utilized in their works.

Despite these advancements, a notable gap exists in understanding the physical mechanisms governing FE small-signal capacitance (SSC) characteristics, specifically correlating capacitance to FE polarization switching and domain configurations. The mechanisms driving the increase of capacitance well below the coercive voltage of ferroelectrics need to be explored. Furthermore, a self-consistent framework capturing the LS hysteresis and SS capacitance characteristics is yet to be developed. Such a framework would facilitate a more comprehensive understanding of the FE capacitance behavior and pave the way for extensive device optimizations.

To address these gaps, we present a multi-grain phase-field simulation framework based on the time-dependent Ginzburg Landau (TDGL) formalism for metal–ferroelectric–insulator–metal (MFIM) capacitors, as it is a basic structure in various FE devices. Our framework captures the large-signal charge (*Q*)–voltage (*V*) hysteresis and the small-signal butterfly *C*–*V* characteristics. The capacitance simulation methodology emulates the experimental process of FE small-signal capacitance (SSC) measurements and unravels the physical mechanisms governing the *C*–*V* response. Focusing on hafnium zirconium oxide ( $\text{Hf}_{0.5}\text{Zr}_{0.5}\text{O}_2$ ) or HZO as the FE material, we explore different components of the capacitive response in the MFIM stacks.

Our analysis unveils two distinct responses behind the butterfly *C*–*V* characteristics:

1. Domain bulk response: the response of regions within the bulk of FE domains.

2. Domain wall response: the response of regions in the domain walls of the FE layer, further comprising two sub-categories:
  - Wide domain wall response at the ferroelectric–dielectric (FE–DE) interface.
  - Domain wall vicinity response.

We delve into the physical aspects of these mechanisms and their contributions to the capacitance characteristics, exploring their dependence on the applied bias voltage and the FE polarization domain configurations. We further compare the mechanisms in the MFIM capacitors with the metal–ferroelectric–metal (MFM) capacitors, whose results are shown in ESI (S1 and S2†). Additionally, we investigate the impact of increasing domain density with ferroelectric thickness scaling on these different components, total FE capacitance, and the capacitive memory window for the CiM applications.

The key contributions of this work include:

- Presenting a self-consistent framework capturing both the large-signal and small-signal FE characteristics.
- Providing insights into the mechanisms governing the butterfly characteristics and the capacitance increase well below the coercive voltage of the FE.
- Correlating FE capacitance to the polarization switching mechanisms (domain growth and domain nucleation) and the domain configurations.

## 2 2D multi-grain phase-field simulation framework

We employ our in-house 2D multi-grain phase-field simulation framework (Fig. 1a), an extension of our previous works,<sup>33,34</sup> to simulate the FE small-signal capacitance (SSC) of the MFIM stacks (Fig. 1c). This framework, based on the time-dependent Ginzburg Landau (TDGL) formalism and grain growth equation,<sup>35</sup> captures the multi-domain *P*-switching in the FE layer while incorporating the polycrystalline nature of HZO.

Polycrystallinity introduces spatial variations in material properties and polarization switching across the FE layer, resulting in the smooth and gradual polarization switching observed experimentally. Grain boundaries in polycrystalline structures act as pinning sites for domain walls, restricting their mobility<sup>36–38</sup> and influencing the capacitance characteristics.<sup>25,26</sup> These effects highlight the necessity of incorporating polycrystallinity into the analysis of SSC characteristics. By explicitly modeling polycrystallinity, we capture the effects of grain structure and boundaries on domain evolution and capacitance trends, addressing a gap in previous works<sup>20,25,29–31</sup> that do not incorporate polycrystalline structure.

Furthermore, HZO exhibits an anisotropic crystal structure, with an alternate polar-spacer (APS) layer configuration along one cross-sectional direction and a fully polar (FP) configuration along the other.<sup>8,39</sup> The low gradient energy ( $\approx 0$ ) associated with the APS stabilizes unit-cell-wide domains, enabling elastically independent polarization switching along this direction.<sup>8,39</sup> This leads to stripe-like polarization domains



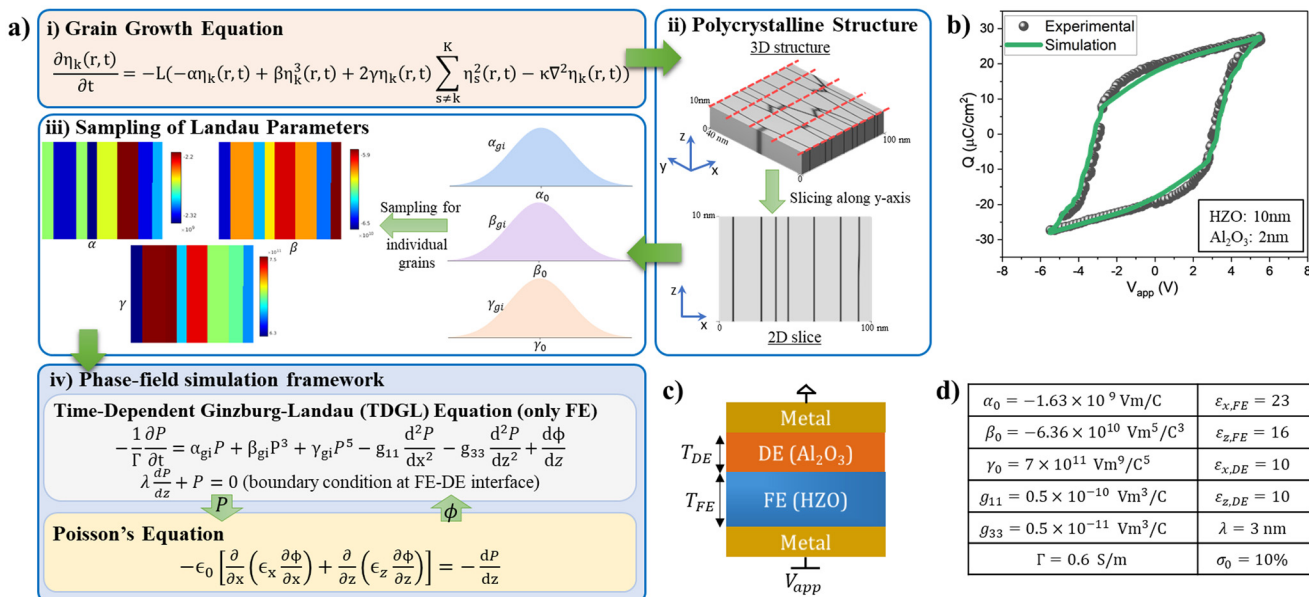


**Fig. 1** (a) 2D multi-grain phase-field simulation framework, illustrating the sequence of steps and equations involved, with arrows indicating the flow of variables across different stages. (b) Comparison of experimental charge ( $Q$ ) versus applied voltage ( $V_{app}$ ) characteristics from Li *et al.*<sup>42</sup> and simulated results (averaged over 20 samples) for MFIM stack with 10nm HZO ferroelectric layer and 2nm  $\text{Al}_2\text{O}_3$  dielectric layer. (c) Reference MFIM structure. (d) List of calibrated parameters and their values for the 2D phase-field simulation framework.

along the APS direction, as validated by first-principles simulations<sup>39</sup> and recent experimental studies,<sup>40,41</sup> particularly for the dimensions of Atomic Layer Deposited (ALD) HZO layer considered in this study.

Given these findings and the significant computational cost of the 3-dimensional (3D) phase-field simulations for the time-scale of SSC measurements, we adopt 2-dimensional (2D) phase-field simulations. These 2D simulations focus on the fully polar (FP) and thickness directions of HZO and we believe these simulations reasonably approximate the MFIM capacitor's behavior.

It may be noted that a polycrystalline structure with different grain orientations could disrupt stripe-like domains across grains (Fig. S3a†). However, the 2D simulation methodology followed in this work represents a special case where the orientation of FP and APS layers align across the grains (Fig. S3b†). One can study this structure to understand the trends in capacitive behavior with the inter-grain variations incorporated in terms of Landau parameters.

The polycrystallinity of HZO is modeled by the grain growth equation (Fig. 1a.i),<sup>35</sup> which captures the spatial and temporal evolution of the polycrystalline microstructure during crystallization, in terms of multiple abstract order parameters ( $\eta_k$ ,  $0 \leq k \leq K$ ) as in eqn (1):

$$\begin{aligned} \frac{\partial \eta_k(r,t)}{\partial t} &= -L(-a\eta_k(r,t) + b\eta_k^3(r,t) \\ &+ 2c\eta_k(r,t) \sum_{s \neq k}^K \eta_s^2(r,t) - \kappa\nabla^2\eta_k(r,t)) \end{aligned}$$

Here,  $r$  represents spatial coordinates and  $t$  represents time. The unitless parameters  $a = 1$ ,  $b = 1$ ,  $c = 1$ ,  $L = 1$ ,  $\kappa =$

0.5, and  $K = 20$  are calibrated to match the grain diameter distributions of simulated polycrystalline structures with experimental data<sup>43</sup> for different HZO film thicknesses. Detailed calibration results are presented in our earlier work.<sup>44</sup>

The abstract parameters ( $\eta_k$ ) represent variations across the grains in the polycrystalline structure, which can differ in properties, such as crystal orientation, material parameters, phase, and strain. In this work, we incorporate this inter-grain variability by considering spatial variations in the parameters of the TDGL equation, as discussed later.

To utilize the 3D polycrystalline structures generated by the grain growth equation in the 2D phase-field model, we extract the  $x$ - $z$  slices (Fig. 1a.ii) of the 3D structure. The 3D structures, measuring  $100 \text{ nm} \times 40 \text{ nm} \times 10 \text{ nm}$ , are sliced along the  $y$ -axis, resulting in 2D  $x$ - $z$  slices of  $100 \text{ nm} \times 10 \text{ nm}$ . Only the 2D slices with unique grain configuration are considered for FE HZO layer and each corresponds to one MFIM sample. In this study, we analyze the characteristics of 50 such unique MFIM samples.

The 2D phase-field framework (Fig. 1a.iv) models electrostatics and polarization ( $P$ ) switching behavior of the MFIM stacks, accounting for the polycrystalline nature of the FE layer. The framework computes the potential  $\phi$  and polarization  $P$  profiles by solving the time-dependent Ginzburg Landau (TDGL) and Poisson's equations. These equations are iteratively and self-consistently solved in 2D real space using a finite difference method with a grid spacing of  $0.5 \text{ nm}$ .<sup>33,44</sup>

The TDGL equation governs the dynamics of polarization switching in the FE layer, relating the rate of change in polariz-

ation ( $P$ ) to the total energy of the system ( $F$ ), given in its Euler-Lagrange form by eqn (2).

$$-\frac{1}{\Gamma} \frac{dP}{dt} = \frac{dF}{dP} \quad (2)$$

The total energy ( $F$ ), includes free energy ( $F_{\text{free}}$ ), electrostatic energy ( $F_{\text{elec}}$ ), and gradient energy ( $F_{\text{grad}}$ ) components in  $x$ - and  $z$ -directions; details of each of the energy components can be found in other work.<sup>33,45</sup> Substituting these individual energy components in eqn (2) results in:

$$-\frac{1}{\gamma} \frac{dP}{dt} = \alpha_{gi} P + \beta_{gi} P^3 + \gamma_{gi} P^5 - g_{11} \frac{\partial^2 P}{\partial x^2} - g_{33} \frac{\partial^2 P}{\partial z^2} + \frac{d\phi}{dz} \quad (3)$$

Here,  $\Gamma$  is the viscosity coefficient,  $\alpha$ ,  $\beta$ ,  $\gamma$  are the Landau free energy parameters, and  $g_{11}$ ,  $g_{33}$  are the gradient energy coefficients along the  $x$ - and  $z$ -directions, respectively.

To account for the inter-grain variability in the polycrystalline HZO layer, we introduce spatial variations in the Landau parameters ( $\alpha$ ,  $\beta$ ,  $\gamma$ ) across grains. For each grain ( $g_i$ ), the values  $\alpha_{gi}$ ,  $\beta_{gi}$  and  $\gamma_{gi}$  are sampled from Gaussian distributions centered around mean values ( $\alpha_0$ ,  $\beta_0$  and  $\gamma_0$ ), with a standard deviation ( $\sigma_0$ ), as shown in Fig. 1a.iii. The mean values and standard deviation are calibrated based on experimental  $Q$ - $V$  results.

Additionally, we account for the surface energy at the FE-DE interface *via* the extrapolation length formalism,<sup>46</sup> resulting in the boundary condition given by:

$$\lambda \frac{\partial P}{\partial z} + P = 0 \quad (4)$$

where  $\lambda$  is the extrapolation length.

Poisson's equation (eqn (5)) describes the electrostatic behavior of the MFIM system in terms of the electrostatic potential ( $\phi$ ).

$$-\epsilon_0 \left[ \frac{\partial}{\partial x} \left( \epsilon_x \frac{\partial \phi}{\partial x} \right) + \frac{\partial}{\partial z} \left( \epsilon_z \frac{\partial \phi}{\partial z} \right) \right] = -\frac{\partial P}{\partial z} \quad (5)$$

Here,  $\epsilon_0$  represents the vacuum permittivity,  $\epsilon_x$  and  $\epsilon_z$  represent the relative material permittivity in the  $x$ - and  $z$ -directions, respectively. The right-hand side of eqn (5) accounts for the bound charges arising from the polarization gradients in the FE layer.

This framework captures polarization switching *via* domain growth and domain nucleation mechanisms in polycrystalline FE layers with non-uniform grain sizes and shapes. For simplicity, we focus on the orthorhombic phase of HZO and its ferroelectric behavior, despite the polymorphic nature of HZO, which includes monoclinic, orthorhombic and tetragonal phases.<sup>47</sup> Extending the model to account for these multiple phases, and the Zr-doping dependent phase concentration,<sup>47,48</sup> would require modifying the TDGL equation using Kittel's approach<sup>49</sup> to capture both polar and anti-polar modes.<sup>48,50,51</sup>

In our simulations, we neglect leakage currents, which is reasonable given the thickness of the simulated MFIM stacks.

We assume uniform strain and no inter-grain elastic interactions ( $g_{11} = 0$  at the grain boundaries)<sup>52–54</sup> as grain boundaries inhibit the continuation of domains unless specific symmetry conditions are satisfied.<sup>37,38</sup> We consider trap/defect-free interfaces. Defects and traps at the interfaces or grain boundaries significantly impact polarization switching<sup>48</sup> by inducing domain pinning,<sup>55,56</sup> leading to asymmetric capacitance characteristics.<sup>28,57</sup> Since our study primarily focuses on symmetric  $C$ - $V$  butterfly curves, we disregard the influence of defects/traps. As we will demonstrate, the characteristic features of the symmetric small-signal  $C$ - $V$  curves can be obtained without invoking traps.

We calibrate our framework using the experimental data from Li *et al.*<sup>42</sup> for MFIM stacks with a 10 nm HZO FE layer and a 2 nm  $\text{Al}_2\text{O}_3$  DE layer. To ensure robust calibration and account for polycrystallinity-induced device-to-device variations, we match the average  $Q$ - $V$  characteristics of 20 simulated MFIM samples with experiments. The calibration of Landau parameters ( $\alpha$ ,  $\beta$ ,  $\gamma$ ) involves determining the mean values ( $\alpha_0$ ,  $\beta_0$ ,  $\gamma_0$ ) and the standard deviation ( $\sigma_0$ ) of the Gaussian distribution from which individual grain parameters are sampled.

For  $\Gamma$ , we use a previously calibrated value of  $0.6 \text{ S m}^{-1}$ .<sup>33</sup> While this choice may affect the capacitance trends at high frequencies, we expect minimal impact on the capacitance and underlying physical mechanisms at the frequency of 1 MHz considered in this study. The final calibrated parameters of the 2D multi-grain phase-field simulation framework are summarized in Fig. 1d, alongside a comparison of simulated and experimental  $Q$ - $V$  characteristics in Fig. 1b. Calibration and comparison of experimental and simulated characteristics for MFM stacks is shown in Fig. S1b and c.†

### 3 Ferroelectric small-signal capacitance: simulation methodology

Using the phase-field framework, we simulate the ferroelectric small-signal capacitance (SSC) by replicating experimental  $C$ - $V$  measurement methodologies.<sup>31</sup> To calculate the capacitance at a given DC bias voltage ( $V_0$ ), we simulate the MFIM stack under this bias  $V_0$  until it reaches a steady state (Fig. 2a). Steady state is defined as the condition where the normalized change polarization of the sample is less than  $10^{-4}\%$ . Once a steady state is achieved, we superimpose a small-signal sinusoidal waveform ( $V_{\text{sin}}$ ) with 1 MHz frequency and 1 mV amplitude onto the DC bias and simulate the response of the MFIM stack under this combined waveform ( $V_0 + V_{\text{sin}}$ ).

The charge response of the MFIM stack to  $V_0 + V_{\text{sin}}$  consists of reversible and irreversible components,<sup>31,32</sup> depending on the proximity of  $V_0$  to the sample's coercive voltage ( $\pm V_c$ ).

- When  $V_0$  falls in non-switching regions of  $Q$ - $V$  (e.g.,  $V_{01}$  in Fig. 2b), far from  $\pm V_c$ , the small-signal charge response is purely reversible (Fig. 2d). This response arises primarily from the background permittivity of the materials and the oscil-



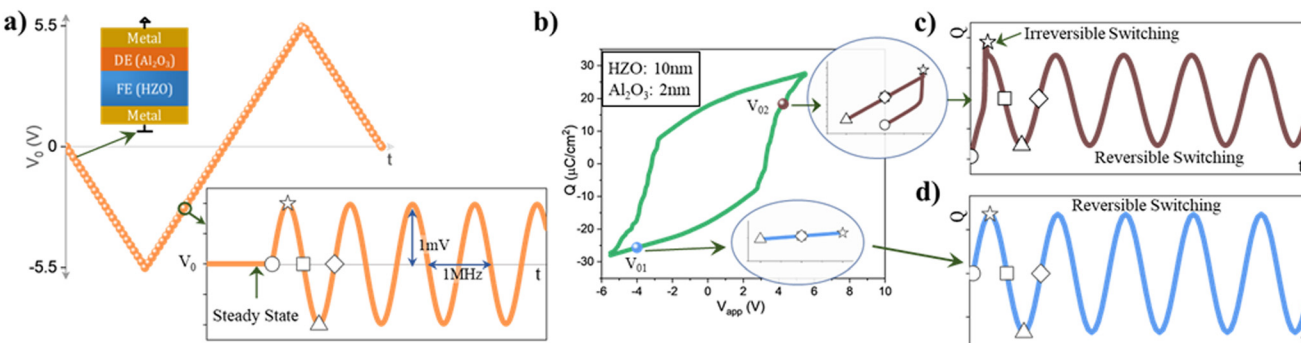


**Fig. 2** (a) Voltage waveform for simulating capacitance–voltage ( $C$ – $V$ ) characteristics of the MFIM stack comprising a large-signal bias voltage ( $V_0$ ) superimposed with a small-signal sinusoidal waveform. (b)  $Q$ – $V$  loop of MFIM stack showing the capacitor's charge response at different bias voltages ( $V_{01}$  and  $V_{02}$ ) in the insets. Small-signal charge response at a bias voltage of (c)  $V_{02}$ , highlighting the initial irreversible response followed by reversible responses, and (d)  $V_{01}$ , where only reversible response is observed.

lation of  $P$ -magnitude in the FE layer, without involving hysteretic  $P$ -switching.

When  $V_0$  is in switching regions of the  $Q$ – $V$  loop (e.g.,  $V_{02}$  in Fig. 2b), near  $\pm V_C$ , the charge response involves both reversible and irreversible components. During initial cycles of  $V_{\text{sin}}$ , an irreversible component appears due to hysteretic  $P$ -switching (inset for  $V_{02}$  in Fig. 2b). However, after a few cycles, the irreversible switching diminishes, leaving only the reversible component (Fig. 2c).

We calculate the small-signal capacitance ( $C$ ) solely from the reversible charge response as the ratio of the amplitude of the reversible charge ( $Q_{\text{sin}}$ ) to the applied sinusoidal voltage ( $V_{\text{sin}}$ ) amplitude:

$$C = \frac{\text{ampl}(Q_{\text{sin}})}{\text{ampl}(V_{\text{sin}})} \Big|_{V_0} \quad (6)$$

To generate the butterfly  $C$ – $V$  curves (Fig. 3a), we vary  $V_0$  in steps of 50 mV, covering the forward ( $-5.5$  V to  $5.5$  V) and backward ( $5.5$  V to  $-5.5$  V) paths. The capacitance at each voltage step is calculated using eqn (6) (Fig. 2a).

The small dimensions of the simulated MFIM samples (width of 100 nm) limit the number of grains in the FE layer. This results in sharp step transitions in the  $Q$ – $V$  loops and multiple peaks and valleys in the  $C$ – $V$  curves. To smooth these  $C$ – $V$  characteristics, we average the  $C$ – $V$  responses across 50 MFIM samples, each with a unique polycrystalline HZO layer. This approach also captures the effects of polycrystalline HZO on the  $C$ – $V$  characteristics.

## 4 Ferroelectric small-signal capacitance: components

The simulation methodology used in this work is generic and applicable to a wide range of FE and DE thicknesses. However, since the phase-field framework has been calibrated for MFIM stacks with 10 nm HZO and 2 nm  $\text{Al}_2\text{O}_3$ , we focus on these specific thicknesses to investigate the mechanisms governing

SSC characteristics over the next two sections. Additionally, we explore the capacitance trends for other FE thicknesses, such as 7 nm and 5 nm. For comparison, we also present the results for MFM stacks with 10 nm HZO in Fig. S1 and S2.† The simulated average  $C$ – $V$  results of these MFIM stacks (Fig. 3a) as well as MFM (Fig. S1d†) successfully replicate the butterfly characteristics observed in experiments.<sup>31,41,42,47,58–60</sup> To better understand the mechanisms governing these characteristics, we divide the total capacitance into dielectric and polarization capacitance components.

Let us approach this division from the perspective of the total charge ( $Q$ ) of the MFIM stack. It is evident that the HZO and  $\text{Al}_2\text{O}_3$  (dead layers in MFM) layers, being in series, hold the same charge  $Q$ . In the HZO layer,  $Q$  embodies the combined effect of two phenomena: the background permittivity response, referred to as the dielectric component ( $Q_{\text{de}}$ ), and the response of the FE polarization domains to the electric field, or the polarization component ( $Q_{\text{p}}$ ). These components sum up to produce the total dielectric response in the  $\text{Al}_2\text{O}_3$  layer. Note, we can attribute a portion of  $Q$  in the  $\text{Al}_2\text{O}_3$  layer (or the dead layers) as a response to the electric field/displacement of the FE dielectric component and the remaining portion as a response to the FE polarization component.

The dielectric ( $Q_{\text{de}}$ ) and polarization ( $Q_{\text{p}}$ ) components of  $Q$  are calculated using the  $z$ -directed electric field ( $E_{z,\text{FE,avg}}$ ) in the FE layer, averaged along the  $x$ -direction.<sup>61</sup>

$$Q_{\text{de}} = \epsilon_0 \epsilon_{z,\text{FE}} E_{z,\text{FE,avg}}$$

$$Q_{\text{p}} = Q - Q_{\text{de}} \quad (7)$$

$E_{z,\text{FE,avg}}$  is determined from the average potential difference between the top interface of the FE layer (at  $\text{Al}_2\text{O}_3/\text{HZO}$ ,  $V_{\text{FE,top,avg}}$ ) and the bottom interface (at  $\text{HZO/metal}$ ,  $V_{\text{FE,bot,avg}}$ ) as in Fig. 3c.

$$E_{z,\text{FE,avg}} = \frac{V_{\text{FE,top,avg}} - V_{\text{FE,bot,avg}}}{T_{\text{FE}}} \quad (8)$$

Here,  $T_{\text{FE}}$  is the thickness of the FE layer.



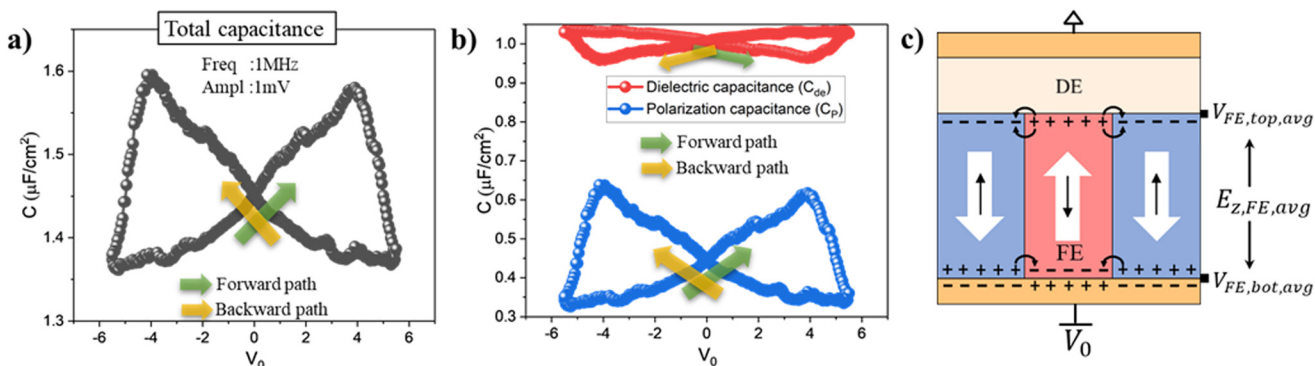


**Fig. 3** (a) Simulated capacitance–voltage ( $C$ – $V$ ) characteristics for MFIM, averaged over 50 samples, with a 10 nm HZO FE layer and 2 nm  $\text{Al}_2\text{O}_3$  dielectric layer. (b) Dielectric ( $C_{\text{de}}$ ) and polarization ( $C_{\text{p}}$ ) capacitance components versus bias voltage, exhibiting inverted butterfly and butterfly characteristics respectively. (c) Schematic of MFIM structure, depicting multi-domain polarized FE layer with depolarization field and in-plane stray fields near domain walls at the FE–DE interface. Also shown are the average voltages on the top ( $V_{\text{FE},\text{top},\text{avg}}$ ) and bottom ( $V_{\text{FE},\text{bot},\text{avg}}$ ) interfaces of the FE layer used to calculate the average out-of-plane electric field ( $E_{z,\text{FE},\text{avg}}$ ).

Analogous to total charge ( $Q$ ), the total capacitance ( $C$ ) can be divided into dielectric ( $C_{\text{de}}$ ) and polarization ( $C_{\text{p}}$ ) capacitance components. These are calculated using the corresponding sinusoidal responses of dielectric ( $Q_{\text{de,sin}}$ ) and polarization ( $Q_{\text{p,sin}}$ ) charge components.

$$C_{\text{de}} = \frac{\text{ampl}(Q_{\text{de,sin}})}{\text{ampl}(V_{\text{sin}})} \Big|_{V_0} \quad (9)$$

$$C_{\text{p}} = \frac{\text{ampl}(Q_{\text{p,sin}})}{\text{ampl}(V_{\text{sin}})} \Big|_{V_0} \quad (10)$$

As shown in (Fig. 3b),  $C_{\text{de}}$  exhibits an inverted butterfly shape and  $C_{\text{p}}$  displays the characteristic butterfly shape.  $C_{\text{p}}$  is mainly responsible for the overall butterfly capacitance characteristics. Similar characteristics are observed for MFM stacks (Fig. S1e†). In the following subsections, we analyze these capacitance components in detail, highlighting the underlying physical mechanisms utilizing the spatial profiles of polarization  $P(x, z)$  and electric-field  $E(x, z)$  of a representative MFIM sample at different bias voltages ( $V_0$ ).

## 5 The dielectric capacitance component

The dielectric capacitance ( $C_{\text{de}}$ ) arises from the background permittivity response of the MFIM stack to  $V_{\text{sin}}$ . This component (from eqn (9)) depends on the out-of-plane or  $z$ -directed electric field in MFIM and exhibits an inverted butterfly shape (Fig. 4a).

To understand this behavior, let us discuss the formation of multi-domains in the FE layer (Fig. 3c) and its impact on  $E$ -field distribution. Imperfect screening of the polarization charges at the FE–DE interface generates a depolarization field—an electric field opposite to the  $P$  direction in the FE layer. This depolarization field increases the electrostatic energy ( $E_{\text{elec}}$ ) of the system, which ferroelectrics often minimize by

breaking into multiple domains with opposite  $P$  directions (Fig. 3c), albeit at the cost of increased gradient energy.<sup>45</sup> This multi-domain structure compensates the  $E$ -field lines originating from one domain in the adjacent oppositely polarized domains. This leads to in-plane  $E$ -fields or stray fields near domain walls (DW) at the FE–DE interface and reduces the out-of-plane  $E$ -field (Fig. 3c) and electrostatic energy.<sup>45</sup>

The strength of in-plane  $E$ -fields is proportional to the number of DWs in the FE layer. Moreover, this strength is maximized when the magnitudes of  $+P$  and  $-P$  domains across a DW are balanced.<sup>62</sup> Variations in the relative magnitudes of these domains with changing bias voltage cause a redistribution of  $E$ -field between in-plane and out-of-plane directions. Since  $C_{\text{de}}$  depends on the out-of-plane  $E$ -field and the resulting induced charges on the metal electrodes, an increase in the in-plane  $E$ -field reduces  $C_{\text{de}}$ .

Let us discuss  $C_{\text{de}}$  versus  $V_0$  focusing on the forward voltage path, where  $V_0$  increases from  $-5.5$  V to  $5.5$  V (Fig. 4a). Starting at  $-5.5$  V, the high negative bias stabilizes the majority of the FE layer in  $-P$  (blue regions in Fig. 4b), with fewer  $+P$  regions (red regions in Fig. 4b). This leads to fewer DWs and asymmetry in the domain magnitudes, with the magnitude of  $-P$  greater than  $+P$  domains. Consequently, most of the  $E$ -field is in the out-of-plane direction, with minimal in-plane components (inset of Fig. 4b), resulting in large  $C_{\text{de}}$ .

As  $V_0$  gradually increases, the magnitude of  $+P$  domains increases while that of  $-P$  domains decreases. This reduces the asymmetry between  $+P$  and  $-P$  domains (Fig. 4c) and allows for greater  $E$ -field compensation near the DWs. In other words, some out-of-plane  $E$ -field transforms to in-plane  $E$ -field (op-to-ip transformation), lowering  $C_{\text{de}}$  with increasing  $V_0$  (Fig. 4a). Due to the absence of multi-domain structure in MFM (Fig. S2a†) at high negative voltages,  $C_{\text{de}}$  does not show a significant decrease in MFM stacks until domain nucleation.

As  $V_0$  increases further and approaches coercive voltage ( $+V_C$ ), the FE layer undergoes  $P$ -switching through domain growth and domain nucleation (Fig. 4d). The nucleation of



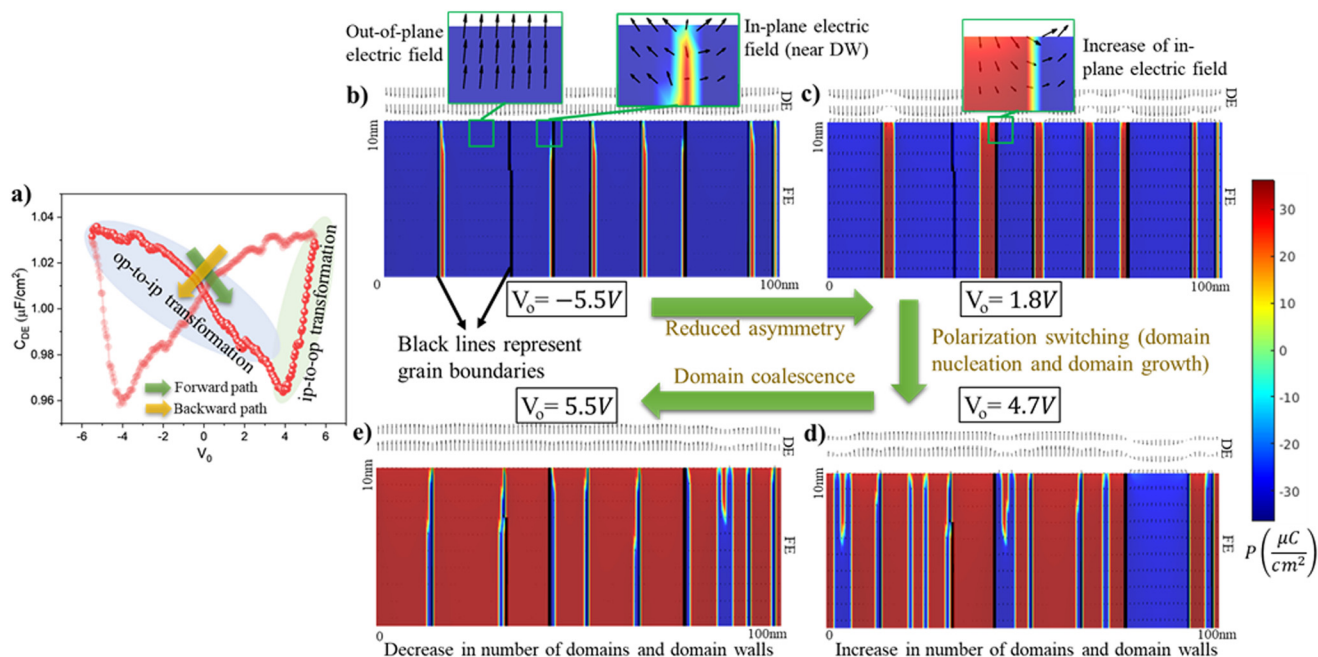


**Fig. 4** (a) Dielectric capacitance ( $C_{DE}$ ) characteristics during the forward path, illustrating the inverted butterfly shape and the associated  $E$ -field transformations. Polarization and electric field profiles along the forward path at specific bias voltages of (b)  $V_0 = -5.5$  V, showing the smaller number of domains in the FE layer, with the inset highlighting lower in-plane  $E$ -field near DWs. (c)  $V_0 = 1.8$  V, with inset indicating an increase in the in-plane electric field component. (d)  $V_0 = 4.7$  V, displaying an increased number of domains and domain walls, leading to a stronger in-plane  $E$ -field, and (e)  $V_0 = 5.5$  V, showing the coalescence of  $+P$  domains, resulting in the reduction of the number of domain walls.

new  $+P$  domains increases the number of domains and DWs in the FE layer, enhancing the in-plane  $E$ -field at the FE-DE interface, leading to a continued decrease in  $C_{DE}$  (Fig. 4a). Note that, the grain boundaries restrict the domain growth (Fig. 4d), inhibiting the propagation or continuation of domains across them, thereby pinning the domain wall at the grain boundaries. This occurs unless specific conditions related to crystallographic symmetry, the relative orientation of the two grains, and the orientation of grain boundary plane are satisfied.<sup>36–38</sup>

As  $V_0$  increases beyond  $+V_C$ , the  $-P$  domains thin and collapse, coalescing  $+P$  domains (Fig. 4e). This reduces the number of DWs in the FE layer, decreases the in-plane  $E$ -field and increases the out-of-plane  $E$ -field (ip-to-op transformation). This change in the  $E$ -field distribution in the MFIM increases  $C_{DE}$  with  $V_0 > +V_C$  (Fig. 4a).

Similar mechanisms, but in the opposite direction, govern  $C_{DE}$  along the backward voltage path. As  $V_0$  decreases from 5.5 V, the reduced asymmetry between  $+P$  and  $-P$  domains increases the in-plane  $E$ -field, decreasing  $C_{DE}$ . As  $V_0$  decreases further and approaches  $-V_C$ , the nucleation of  $-P$  domains boosts the in-plane  $E$ -field, further reducing  $C_{DE}$ . Finally, as  $V_0$  falls below  $-V_C$ , the coalescence of  $-P$  domains reduces the in-plane  $E$ -field and increases the out-of-plane  $E$ -field and  $C_{DE}$ . This interplay between in-plane and out-of-plane  $E$ -field transformations,  $P$ -switching *via* domain nucleation and coalescence, and the evolution of  $P$ -domain configurations results in the inverted butterfly characteristics of the dielectric capacitance component shown in Fig. 4a.

## 6 The polarization capacitance component

The polarization capacitance ( $C_P$ ) arises from the response of FE polarization domains to the sinusoidal waveform and exhibits butterfly shape (Fig. 3b). Our analysis reveals two physical responses governing  $C_P$  characteristics across  $V_0$ :

1. Domain bulk response: This refers to the response of the FE regions deep within the polarization domains, away from the domain walls (DWs).

2. Domain wall response, which comprises:

- Wide domain wall response: The response of wide domain walls or the “softer” domains near the FE-DE interface.

- Domain wall vicinity response: This refers to the response of the FE regions adjacent to DWs.

Given the small amplitude of the sinusoidal voltage (1 mV), it is difficult to discern the small signal response directly in the polarization profiles of the FE layer. To illustrate these small changes in  $P$ , we utilize the polarization-amplitude (ampl- $P$ ) profiles (Fig. 5b) that depict the minute polarization response to  $V_{\sin}$ . For any bias voltage, the polarization-amplitude profiles are obtained by spatially subtracting the polarization at the time when  $V_{\sin}$  is zero ( $t_0$ ) from the polarization at the peak of the  $V_{\sin}$  ( $t_{\max}$ ), as in Fig. 5a and eqn (11).

$$\text{ampl-}P(x, z) = P(x, z, t_{\max}) - P(x, z, t_0) \quad (11)$$

To quantify the contributions of the domain bulk and domain wall responses, we define averaged domain bulk



capacitance ( $C_{DB}$ ) and averaged domain wall capacitance ( $C_{DW}$ ), capturing the respective responses. Since these responses are spatially distributed, we partition the FE layer into domain bulk (DB) and domain wall (DW) regions based on  $P$ -magnitude and gradient energy. DW regions are characterized by lower  $P$ -magnitude and higher gradient energy than the DB regions. In the considered MFIM configuration, we typically observe hard or sharp DWs<sup>45</sup> with no lattice points in the  $P$  transition region. For calculating  $C_{DW}$ , lattice points on either side of the  $P$ -transition are included into the DW region, resulting in a DW width of 2 lattice points for hard DWs. Under certain conditions (discussed in section 6.2.1), softer DWs with widths greater than 2 lattice points are observed.

The averaged capacitances ( $C_{DB}$  and  $C_{DW}$ ) are calculated at each  $V_0$  by spatially aggregating the ampl- $P$  of the DB and DW regions. This aggregated value is then normalized with the sinusoidal voltage amplitude (ampl( $V_{sin}$ ) = 1 mV) and the area of the FE layer in  $x$ - $z$  plane (Area = 100 nm × 10 nm), as follows:

$$C_{DB} = \frac{\sum_x \sum_z \text{ampl-}P_{DB}(x, z)}{\text{ampl}(V_{sin})} * \frac{1}{\text{Area}} \quad (12)$$

$$C_{DW} = \frac{\sum_x \sum_z \text{ampl-}P_{DW}(x, z)}{\text{ampl}(V_{sin})} * \frac{1}{\text{Area}} \quad (13)$$

Here, ampl- $P_{DB}(x, z)$  and ampl- $P_{DW}(x, z)$  represent the polarization-amplitude of the domain bulk and domain wall regions, respectively.

## 6.1 Domain bulk (DB) response

Domain bulk regions, characterized by low gradient energy, comprise both  $+P$  and  $-P$  domains. The minimal gradient energy implies that the polarization of DB regions is governed by the Landau–Khalatnikov (LK) equation, which

accounts for  $F_{free}$  and  $F_{elec}$  contributions of the FE material (eqn (14))

$$E = \alpha P + \beta P^3 + \gamma P^5 \quad (14)$$

The LK equation exhibits an S-shaped curve with segments of varying slopes—low, moderate, and high (marked in Fig. 6c)—that influence the response of DB regions to  $V_{sin}$  based on their location on the curve.

To illustrate this dependence, we select reference points in the DB regions of the FE layer (green stars in Fig. 6a) and examine their polarization ( $P$ ) *versus* the experienced  $E$ -field calculated from the phase-field model. We refer to this as the  $P$ - $E$  positions of these points and plot them against the S-shaped LK curve (Fig. 6c). Note that the LK curve is constructed using the mean Landau parameters ( $\alpha_0, \beta_0, \gamma_0$ ), while the actual  $P$ - $E$  positions account for the polycrystalline-induced variability ( $\alpha_{gi}, \beta_{gi}, \gamma_{gi}$ ) in the Landau parameters. The slope of the LK curve at each  $P$ - $E$  position determines the response of these DB regions to  $V_{sin}$ .

Starting with the forward voltage path at  $V_0 = -5.5$  V, the FE layer is dominated by  $-P$  regions with thin  $+P$  domains (Fig. 6a). The  $P$ - $E$  positions of the reference DB points (Fig. 6c, -5.5 V) fall in the low-slope segments of the LK curve. This indicates a minimal response of these DB regions to the  $V_{sin}$ , evident from the small ampl- $P$ , approximately  $10^{-4}$   $\mu\text{C cm}^{-2}$  (Fig. 6b). Despite this low response, the large extent of DB regions across the FE layer means their collective contribution to the  $C_P$  remains significant (Fig. 5d) (similarly in MFM Fig. S1f†).

As  $V_0$  increases but remains below  $+V_C$ ,  $P$ -switching is mainly driven by domain growth (Fig. 6d for 1.8 V). The polarization of  $+P$  domains increases, shifting their  $P$ - $E$  positions further into the low-slope segment of the LK curve (Fig. 6c), which diminishes their response to  $V_{sin}$ . On the other hand, the magnitude of  $-P$  domains decreases, shifting their  $P$ - $E$  positions towards the high-slope segment or the turnaround

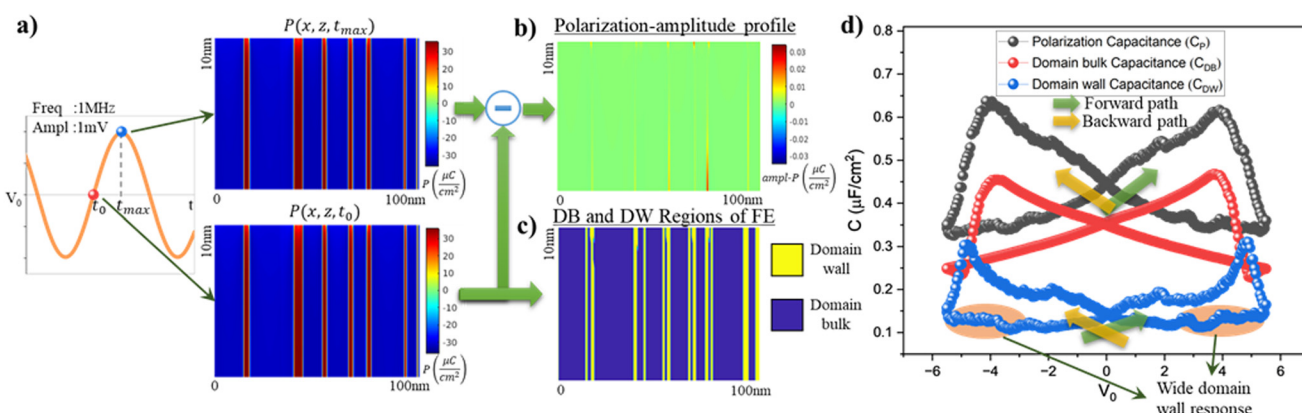
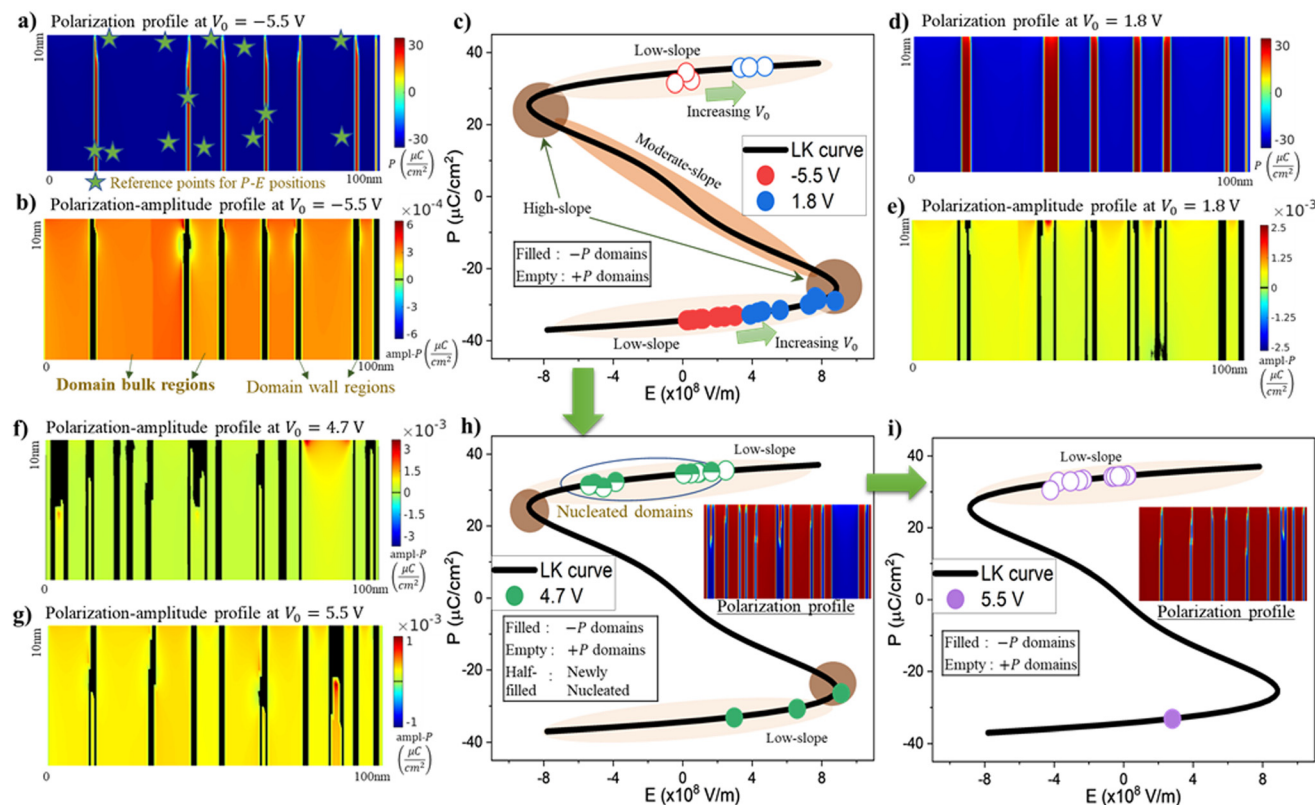


Fig. 5 (a) Method for calculating polarization–amplitude profile of the FE layer at any given bias voltage ( $V_0$ ), obtained by subtracting the polarization profile at the zero-crossing of the sinusoidal waveform ( $t_0$ ) from the polarization profile at sinusoidal peak ( $t_{max}$ ). (b) Polarization–amplitude profile for  $V_0 = 1.8$  V. (c) Division of FE layer into domain wall and domain bulk regions for  $V_0 = 1.8$  V and (d) Polarization capacitance ( $C_P$ ) along with the domain bulk ( $C_{DB}$ ) and domain wall ( $C_{DW}$ ) capacitances *versus* bias voltage.





**Fig. 6** (a) Polarization profile  $P(x, z)$  at  $V_0 = -5.5$  V, with reference points (in green stars) for analysis of  $P-E$  positions. (b) Polarization–amplitude profile  $\text{ampl-}P(x, z)$  at  $V_0 = -5.5$  V, showing the low response of domain bulk regions and the domain wall regions represented in black. (c)  $P-E$  positions of DB reference points plotted on the LK curve for  $V_0 = -5.5$  V and 1.8 V, showing traversal of  $+P$  domains along low-slope and  $-P$  domains towards high-slope segments. (d) Polarization and (e) polarization–amplitude profiles at  $V_0 = 1.8$  V, indicating the increase in the sinusoidal response of the DB regions.  $\text{ampl-}P(x, z)$  at (f)  $V_0 = 4.7$  V, showing a reduction in DB area due to domain nucleation, and (g)  $V_0 = 5.5$  V showing increased DB area due to domain coalescence. (h)  $P-E$  positions of DB reference points for  $V_0 = 4.7$  V, indicating the shift from the high-slope to the low-slope segment of the LK curve due to domain nucleation, with  $P(x, z)$  in the inset. (i)  $P-E$  positions of DB reference points for  $V_0 = 5.5$  V, indicating the shift along the low-slope segment of the LK curve, with  $P(x, z)$  in the inset.

point of the LK curve (Fig. 6c). This increases their response to  $V_{\text{sin}}$  to approximately  $10^{-3} \mu\text{C cm}^{-2}$  (Fig. 6e). Overall,  $C_{\text{DB}}$  increases with  $V_0$  (Fig. 5d) as FE is predominantly negative polarized.

$C_{\text{DB}}$  increases with further increase in  $V_0$  as the  $P-E$  positions of  $-P$  domains move further towards the high-slope segment of the LK curve. As  $V_0$  approaches  $+V_{\text{C}}$ , the  $P-E$  positions of  $-P$  domains reach the turnaround point of the LK curve, where even a slight increase in  $V_0$  switches from  $-P$  to  $+P$  polarization. The switching behavior, however, depends on the proximity of these  $-P$  regions to DWs. Regions near DWs switch *via* domain growth and their capacitive response is discussed in section 6.2.2 (on domain wall vicinity response). The regions away from DWs switch *via* domain nucleation, where new  $+P$  domains nucleate from the FE–DE interface.

The nucleation of  $+P$  domains relocates their  $P-E$  positions to the low-slope segment of the LK curve (Fig. 6h), reducing their response to the sinusoidal waveform. Additionally, nucleation increases the number of domains and DWs in the FE layer, reducing the DB regions (Fig. 6f). Thus, after nuclea-

tion, these two factors lead to a drop in  $C_{\text{DB}}$ , which was previously increasing with  $V_0$ . However, due to averaging over 50 MFIM samples with polycrystalline-induced variations in  $V_{\text{C}}$ , we observe a relatively smooth decrease in  $C_{\text{DB}}$  with  $V_0$ .

With further increase in  $V_0$ , the  $+P$  domains grow and coalesce, reducing the DW area and increasing the DB regions (Fig. 6g). However, the  $P-E$  positions of DB regions now traverse along a low-slope segment of the LK curve (Fig. 6i). This results in only a slight increase in  $C_{\text{DB}}$  at high bias voltages (around 5 V in Fig. 5d).

Similar mechanisms involving the opposite polarization govern the domain bulk capacitance in the backward path. As  $V_0$  decreases from  $+5.5$  V,  $+P$  DB regions move towards the high-slope segment of the LK curve, increasing  $C_{\text{DB}}$ . Subsequently,  $+P$  domains switch to  $-P$  *via* domain nucleation reducing the DB regions, and  $C_{\text{DB}}$  decreases. Following this,  $-P$  domains coalesce, slightly increasing  $C_{\text{DB}}$ . These interactions—traversal along the LK curve by DB regions, polarization switching *via* domain nucleation and coalescence—govern the dependence of domain bulk capacitance ( $C_{\text{DB}}$ ) on bias voltage (Fig. 5d).

## 6.2 Domain wall response

Domain walls (DWs) refer to the transition regions between different polarization directions, in this case,  $+P$  and  $-P$  domains. These DW regions are characterized by high gradient energies due to spatial variations in polarization and a lower (closer to zero)  $P$ -magnitude compared with DB regions. Our analysis identifies two different DW responses to the sinusoidal waveform: wide DW response at the FE-DE interface and DW vicinity response.

In the simulated MFIM structures, DWs are typically sharp or "hard" with a considered width of 2 lattice points. The response of hard DWs to  $V_{\text{sin}}$  is discussed in section 6.2.2 on domain wall vicinity response. However, for certain  $V_0$ , we observe the formation of wide or "softer" DWs near the FE-DE interface. The width of these DWs is greater than 2 lattice points and we refer to the response of these regions as a wide domain wall response at the FE-DE interface, which we discuss next.

### 6.2.1 Wide domain wall response at the FE-DE interface.

At the FE-DE interface, domain walls are typically wider than in the bulk of the FE layer.<sup>63</sup> Under high negative (positive) bias voltages where  $+P$  ( $-P$ ) domains become very thin, we observe further widening of the DWs at the FE-DE interface. These widened DWs, due to their distinct properties, exhibit heightened response to  $V_{\text{sin}}$ , which we refer to as the wide domain wall response at the FE-DE interface (highlighted in Fig. 5d).

Wide DWs at the interface imply a slower transition of polarization to the domain bulk (DB) values compared with the regions away from the interface (FE bulk), as in Fig. 7c. In the FE bulk, DWs are sharp (hard), with  $P$ -magnitude on either side of DW close to DB values. However, at the interface, stray or in-plane  $E$ -fields near the DWs (discussed in section

5, Fig. 3c) reduce the out-of-plane  $E$ -field. This reduction lowers the polarization magnitudes, creating an additional transition zone between the  $+P$  and  $-P$  domains and thereby widening the DWs. This phenomenon is observable at any bias voltage ( $V_0$ ) and has been investigated in prior works<sup>63</sup> and observed in other phase-field simulation works.<sup>61,64</sup>

At high negative (positive) bias voltages, DW widening is more pronounced due to thin  $+P$  ( $-P$ ) domains and strong depolarization fields. For instance, at  $V_0 = -5.5$  V, the thinning of  $+P$  domains (Fig. 7d) reduces the  $+P$  magnitude,<sup>62</sup> even in regions away from the FE-DE interface. At the interface, this reduction of  $+P$  magnitude is intensified by the polarization gradient along  $z$ -direction (Fig. 7b), induced by the depolarization fields. The lower  $+P$  domain magnitude at the interface slows the transition between the  $+P$  and  $-P$  domains, further widening the DWs. As a result, we observe conical  $+P$  ( $-P$ ) domains (Fig. 7d), with DWs near the interface exhibiting "softer" characteristics than those in the FE bulk.

These conical domains form head-to-head or tail-to-tail domain walls near the interface. These domain walls are experimentally observed in HZO<sup>40</sup> and are shown to be stable under certain charge compensation conditions.<sup>65</sup> In our simulations, conical domains are observed near the grain boundaries in the polycrystalline FE (Fig. 7d), where their stability is strongly influenced by the grain boundary effects. These conical  $+P$  ( $-P$ ) domains minimize the energy of the system by compensating the depolarization field from the neighboring  $-P$  ( $+P$ ) domains. This compensation occurs at the cost of gradient energy at only a single domain wall, consistent with our assumption of no inter-grain elastic interactions ( $g_{11} = 0$  at the grain boundaries). Note that, such conical domains are absent in MFM structures due to the lower depolarization field (Fig. S2a and d†). Therefore, the capacitance in the MFM stack

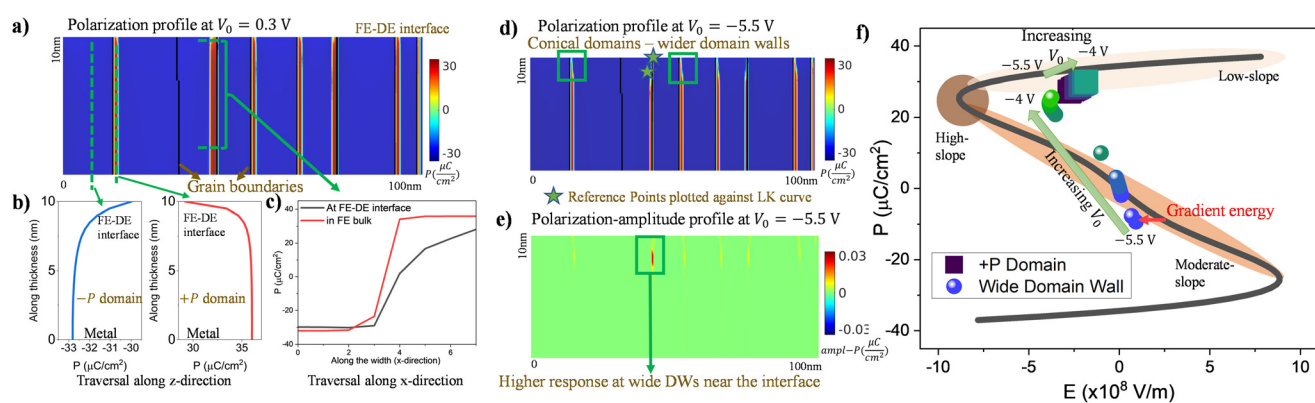


**Fig. 7** (a) Polarization profile at  $V_0 = 0.3$  V with black lines indicating grain boundaries. (b) Line plot of polarization along the thickness ( $z$ -direction) in  $+P$  and  $-P$  domains, illustrating the reduced polarization magnitude at the FE-DE interface compared with away from the interface and the polarization gradient along the  $z$ -direction. (c) Line plot of polarization along the  $x$ -direction crossing a domain wall, showing the widening of DW at the FE-DE interface compared with the FE bulk. (d) Polarization profile at  $V_0 = -5.5$  V highlighting the formation of conical domains at the interface near the grain boundaries and the reference points of plotted  $P$ - $E$  positions in green stars. (e) Polarization-amplitude profile for  $V_0 = -5.5$  V, with a higher response at the wide DWs near the interface. (f) Reference points of  $+P$  domain (squares) and wide DW region (circles) plotted against the LK curve for  $V_0$  increasing from  $-5.5$  V to  $-4$  V, showing the traversal of wide DW point along the moderate-slope to high-slope segment and the  $+P$  domain point moving away from the high-slope segment.



does not have a contribution from the wide domain wall response (Fig. S1f†).

To understand the wide DW response, we focus on the forward voltage path and the  $P$ - $E$  positions of two reference lattice points (green stars in Fig. 7d): one located in the wide DW region and the other in the  $+P$  domain near the interface. At  $V_0 = -5.5$  V, the polarization in wide DW regions transitions gradually between oppositely polarized domains. As a result, their  $P$ - $E$  positions lie along the moderate (negative)-slope segment of the LK curve (circle in Fig. 7f). The position on the negative slope of the LK curve is a localized and steady-state phenomenon that is consistent with the behavior of the softer DW regions reported in previous works.<sup>61,64</sup> On the other hand, the  $P$ - $E$  positions of  $+P$  domains near the interface fall along the high-slope segment (square in Fig. 7f), due to their slightly lower  $P$ -magnitude compared with FE bulk (away from the interface). Note that, these  $P$ - $E$  positions deviate from the LK curve due to the high gradient energy associated with the DW and FE-DE interface regions.

The placement of  $P$ - $E$  positions along the moderate and high-slope segments of the LK curve implies a heightened response to  $V_{\text{sin}}$ . This heightened response, as evident from the ampl- $P$  profile (Fig. 7e), is approximately  $10^{-2}$   $\mu\text{cm}^2$  and is significantly higher than the response of DB regions ( $10^{-4}$   $\mu\text{cm}^2$ ). However, since these regions constitute only a small portion of the FE layer, their aggregate response ( $C_{\text{DW}}$ ) is smaller than that of domain bulk ( $C_{\text{DB}}$ ) (Fig. 5d).

As  $V_0$  increases from  $-5.5$  V, the polarization of  $+P$  domains increases, shifting their  $P$ - $E$  positions towards the low-slope segment of the LK curve (squares in Fig. 7f). Simultaneously, the  $P$ - $E$  positions of wide DW regions at the FE-DE interface traverse along the moderate slope segment towards the high-slope turnaround point (circles in Fig. 7f). However, due to the small area occupied by wide domain walls, domain wall capacitance ( $C_{\text{DW}}$ ) shows minimal variation with increasing the bias voltage ( $V_0$ ).

With the continued increase in  $V_0$ ,  $+P$  domains stabilize and the conical domains transform to more cylindrical shapes, reducing the width of DWs at the FE-DE interface. The previously “softer” (wide) domain walls transition to hard DWs, shifting their  $P$ - $E$  positions to the low-slope segment of the LK curve (circle in Fig. 7f for  $V_0 = -4$  V). This reduces their response to the sinusoidal waveform, causing a slight dip in the domain wall capacitance ( $C_{\text{DW}}$ ), as highlighted in Fig. 5d. With a further increase in  $V_0$ , the regions near the domain walls contribute to the overall response to the sinusoidal waveform, which will be discussed in the next section.

Similarly, at high positive bias voltages ( $V_0 = 5.5$  V), conical  $-P$  domains with wider domain walls at the FE-DE interface exhibit a higher response to the sinusoidal waveform. As  $V_0$  decreases, these conical  $-P$  domains transition to cylindrical domains, reducing DW widening and causing a dip in the domain wall capacitance ( $C_{\text{DW}}$ ). In summary, softer domains at the FE-DE interface with wider domain walls govern the

wide-domain wall response at highly positive and negative bias voltages.

**6.2.2 Domain wall vicinity response.** We define the domain wall vicinity response as the response of the FE regions adjacent to the  $P$ -transition zones, specifically the 2 lattice points considered the DW region. This response occurs across all bias voltages ( $V_0$ ) whenever DWs are present in the FE layer and contributes significantly to the domain wall ( $C_{\text{DW}}$ ) and the polarization ( $C_P$ ) capacitances. The magnitude of this contribution depends on the area by DWs in the FE layer and is strongly influenced by the domain configurations,  $P$ -switching mechanisms, and applied bias voltage.

To understand these dependencies, we focus on the forward voltage path and examine the area surrounding a representative DW in the FE layer (dashed green line in Fig. 8a). The polarization in this region exhibits a sharp transition from  $+P$  to  $-P$  domains (black line in Fig. 8d). Let us consider the lattice points on either side of this region (green and purple markers in Fig. 8d) and examine their  $P$ - $E$  positions over the range of  $V_0$  (2.3 to 2.35 V for the sample being discussed), where this DW undergoes motion or domain growth. Outside this range, the  $P$ - $E$  positions of these points typically fall along the low-slope segment of the LK curve.

At  $V_0 = 2.3$  V, the  $P$ - $E$  position of  $+P$  lattice point (green marker) is along the low-slope segment of the LK curve (Fig. 8e), showing minimal response to  $V_{\text{sin}}$  (Fig. 8d). In contrast, the  $P$ - $E$  position of  $-P$  lattice point (purple marker) is along the high-slope segment (Fig. 8e), exhibiting heightened response of around  $1.5 \times 10^{-2}$   $\mu\text{C cm}^{-2}$  (Fig. 8b, red line in Fig. 8d). This asymmetry in the polarization response between the two sides of the DW leads to a reversible shift in the DW position with the sinusoidal voltage, a phenomenon often referred to as “domain wall vibration” in the literature.<sup>23–26</sup>

A slight increase in  $V_0$  to 2.35 V causes the purple marker (exhibiting heightened response at 2.3 V) to switch to  $+P$  via domain growth or DW motion (Fig. 8f). This switching shifts its  $P$ - $E$  position from the high-slope segment to the low-slope segment (purple marker in Fig. 8g), reducing its response to the sinusoidal waveform (purple marker in Fig. 8f). Meanwhile, the new  $-P$  lattice point (gold marker in Fig. 8f) adjacent to the transition region is still slightly away from the high-slope turnaround point (Fig. 8g). Due to the significant slope variation of the LK curve near the turnaround point, this gold lattice point exhibits a slightly lower sinusoidal response (Fig. 8f), around  $2 \times 10^{-3}$   $\mu\text{C cm}^{-2}$ . Consequently, the small-signal charge response near this DW diminishes at 2.35 V (Fig. 8c and f).

However, numerous DWs are present across the 50 different MFIM samples, with the polycrystalline variations introducing variability in the voltages at which these different DWs respond. Due to the Gaussian distribution of Landau parameters, we observe a Gaussian distribution for the voltages at which different DWs undergo DW motion. Consequently, as  $V_0$  increases, more DWs approach the threshold of the DW motion, continuously increasing  $C_{\text{DW}}$  with  $V_0$  (Fig. 5d).



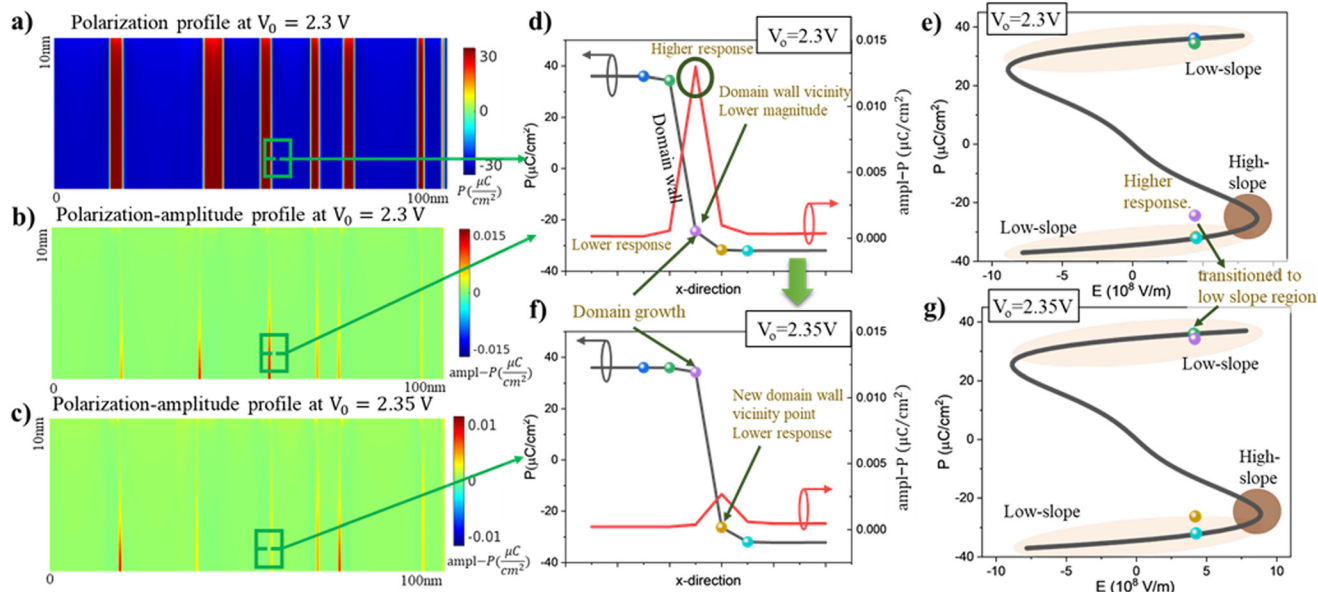


**Fig. 8** (a) Polarization profile and (b) polarization–amplitude profile for  $V_0 = 2.3$  V, showing the high response in the domain wall vicinity regions (green box). (c) Polarization–amplitude profile for  $V_0 = 2.35$  V, after domain growth, showing the reduced response in DW vicinity regions. (d) Line plot of polarization (black) and polarization–amplitude (red) along the  $x$ -direction near the highlighted DW region for  $V_0 = 2.3$  V, with the reference points (circles markers) to be plotted against the LK curve. (e) Reference points plotted against the LK curve for  $V_0 = 2.3$  V, showing the domain wall vicinity point in the high-slope region. (f) Line plot of polarization (black) and polarization–amplitude (red) for  $V_0 = 2.35$  V, illustrating the domain growth and the reduced polarization response. (g) Reference points against the LK curve for  $V_0 = 2.35$  V.

As  $V_0$  approaches the vicinity of coercive voltage ( $+V_c$ ), the FE layer undergoes  $P$ -switching *via* domain nucleation (Fig. 4d). This process increases the number of  $+P$  domains and DWs in the FE layer (Fig. 6f), increasing the domain wall vicinity response. This is evident from the rise of  $C_{\text{DW}}$  after the peak of domain bulk capacitance (which occurs before nucleation) in Fig. 5d. With further increase in  $V_0$ ,  $+P$  domains grow and coalesce (Fig. 4e), reducing the number of DWs in FE. As a result,  $C_{\text{DW}}$  reaches a maximum and starts decreasing with increasing  $V_0$  above  $+V_c$  (Fig. 5d).

Similar mechanisms but with opposite polarization govern  $C_{\text{DW}}$  along the backward path. As  $V_0$  decreases from 5.5 V to  $-5.5$  V,  $-P$  domains stabilize, enhancing the sinusoidal response of the  $+P$  regions near the DWs about to undergo domain growth. As  $V_0$  decreases further, more DWs approach the verge of DW motion, increasing  $C_{\text{DW}}$ . With a further decrease in  $V_0$ ,  $-P$  domains nucleate, increasing the number of DWs and  $C_{\text{DW}}$ . Eventually,  $C_{\text{DW}}$  reaches a peak and decreases due to the coalescence of  $-P$  domains. These interactions between  $P$ -switching *via* domain growth, and the change in the number of DWs *via* domain nucleation and coalescence governs the domain wall vicinity response.

## 7 Ferroelectric small-signal capacitance: summary

Let us summarize the mechanisms behind the butterfly  $C$ – $V$  characteristics. The total ferroelectric capacitance ( $C_{\text{TOT}}$ ) con-

sists of dielectric ( $C_{\text{DE}}$ ) and polarization ( $C_P$ ) capacitance components.  $C_{\text{DE}}$  exhibits an inverted butterfly shape due to the transformation between in-plane and out-of-plane electric fields, which mildly counteracts the butterfly trend of  $C_P$ . In turn,  $C_P$ —the primary driver of the butterfly shape—consists of domain bulk ( $C_{\text{DB}}$ ) and domain wall ( $C_{\text{DW}}$ ) responses, which are influenced by the domain configurations and voltage-dependent polarization switching mechanisms in the FE layer.

Starting from  $V_0$  of  $-5.5$  V and moving along the forward path,  $C_{\text{TOT}}$  increases due to the dominance of  $C_{\text{DB}}$ , as the  $-P$  DB regions shift from low-slope towards high-slope segment of the LK curve. Additionally, wide domain walls at the FE–DE interface due to the formation of conical  $+P$  domains at the grain boundaries contribute to the capacitance response in MFIM stacks. However, this effect diminishes as  $+P$  domains stabilize into cylindrical shapes with increasing  $V_0$ . As  $+P$  domains stabilize with increasing  $V_0$ , the contribution from the DW vicinity response increases, particularly from domains ready for growth. For the simulated configuration of 10 nm HZO with 2 nm  $\text{Al}_2\text{O}_3$ , due to the lower area of DWs, the DW vicinity response is less pronounced compared with the DB response for  $V_0 < +V_c$ .

As  $V_0$  approaches  $+V_c$ , the  $-P$  DB regions reach the high-slope turnaround point of the LK curve, resulting in a peak in  $C_{\text{TOT}}$  near  $+V_c$ . Further increase in  $V_0$  leads to  $P$ -switching *via* nucleation of  $+P$  domains, which increases the area of DWs and reduces domain bulk regions. This causes a decrease in  $C_{\text{DB}}$  while  $C_{\text{DW}}$  increases to a peak value. After certain  $V_0$ ,  $+P$  domains coalesce, reducing the number of domain walls and



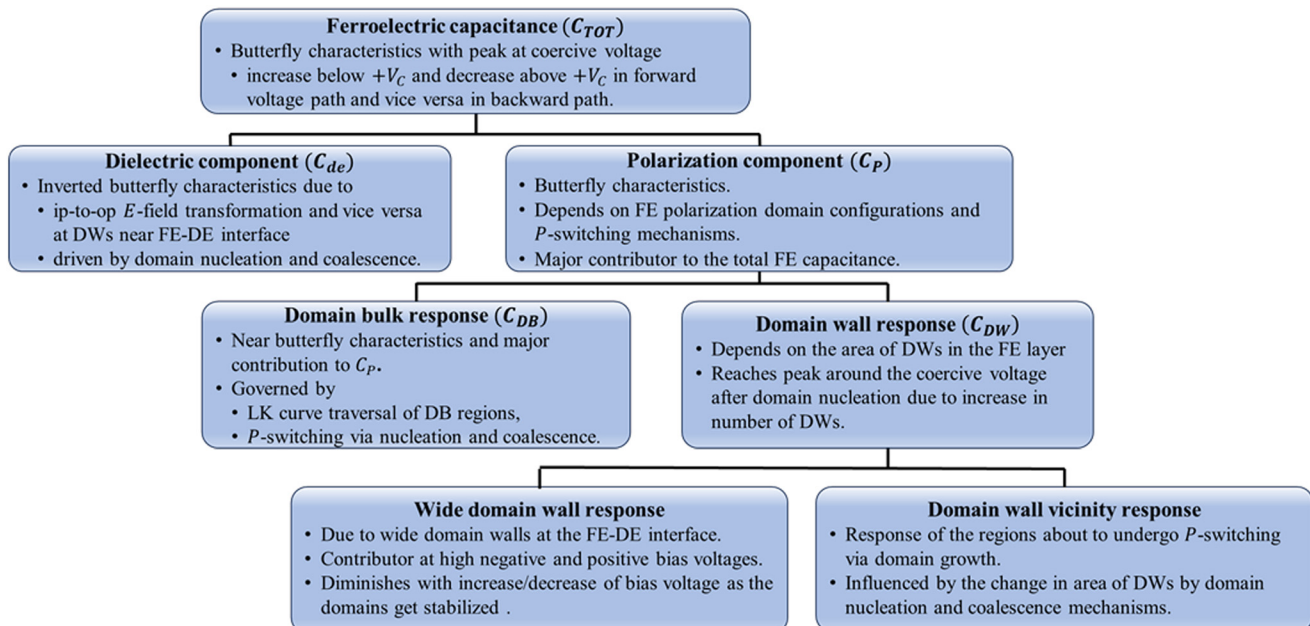


Fig. 9 Summary of different capacitance components and responses in the metal–ferroelectric–insulator–metal (MFIM) capacitors.

$C_{DW}$ .  $C_{DB}$  remains low as  $-P$  DB regions traverse the low-slope regions of the LK curve, thereby reducing  $C_{TOT}$  above  $+V_C$ .

On the reverse path, similar mechanisms lead to an initial increase in the capacitance up to a peak, followed by a decrease. In summary, the voltage-dependent interplay between domain bulk and domain wall responses, alongside polarization switching *via* domain growth, nucleation, and coalescence give rise to the butterfly  $C$ – $V$  characteristics observed in MFIM stacks. Fig. 9 summarizes these different capacitance components.

## 8 Scaling ferroelectric thickness and capacitive memory window

This section examines the impact of scaling the ferroelectric thickness on the small-signal  $C$ – $V$  characteristics. We simulate MFIM stacks with HZO thicknesses of 5, 7, and 10 nm, each paired with a 2 nm  $\text{Al}_2\text{O}_3$  layer. To ensure consistency, the bias voltage range was chosen to maintain a constant electric field across the FE layer at the maximum voltage point for each thickness. Note, we utilize the material and TDGL parameters calibrated for the 10 nm HZO and 2 nm  $\text{Al}_2\text{O}_3$  MFIM sample. However, in practical scenarios, these parameters may vary with FE thicknesses due to strain, processing conditions, and others. Therefore, this section focuses on trends in capacitance behavior with FE thickness scaling rather than absolute capacitance values.

The  $C$ – $V$  characteristics (Fig. 10a) exhibit a butterfly shape across different FE thicknesses, with the total capacitance increasing as FE thickness scales down.<sup>59,60</sup> As discussed in Section 4, the total capacitance can be divided into the dielectric capacitance ( $C_{DE}$ ) component with an inverted butterfly

shape and the polarization capacitance ( $C_P$ ) with butterfly characteristics (Fig. 10b and c). Both  $C_{DE}$  and  $C_P$  increase with reducing FE thickness and we observe an expanded range of capacitance across bias voltage. Although the overall increase in capacitance partly results from reduced device thickness, our analysis shows that the polarization domain configurations also play a crucial role in this trend.

Scaling down FE thickness increases the polarization domain density in the FE layer (Fig. 11a, b and c) due to the interplay between gradient and electrostatic energy, as demonstrated by previous studies.<sup>44,62</sup> Higher domain density increases the area of DWs and reduces the DB regions. As a result,  $C_{DB}$  decreases with FE thickness scaling (Fig. 10d), while  $C_{DW}$  increases (Fig. 10e). The increase in  $C_{DW}$  is larger than the decrease in  $C_{DB}$  since DW regions lie on the high-slope segment of the LK curve, while DB regions generally fall into low-slope segments except on the verge of domain nucleation. Consequently,  $C_{DW}$  contributes significantly to  $C_P$  at lower FE thicknesses, leading to an additional component of the increase in  $C_P$  with FE thickness scaling.

As FE thickness decreases, the increased domain density shifts the  $P$ -switching mechanism from a combination of domain growth and domain nucleation (at higher FE thicknesses) to predominantly domain growth (at lower FE thicknesses) (Fig. 11).<sup>62</sup> As a result, at lower FE thickness, with more domain walls positioned for domain growth at a given bias voltage, especially near coercive voltage, we observe higher maximum  $C_{DW}$  and thus a larger range of  $C_{DW}$  and  $C_P$ .

Examining  $C_{DE}$  trends across FE thickness, we observe that increased domain density with FE thickness scaling enhances in-plane  $E$ -field (and reduces out-of-place  $E$ -fields), which lowers the charge response of the ferroelectric. As a result,  $C_{DE}$  shows a lower increase with FE thickness scaling than it would



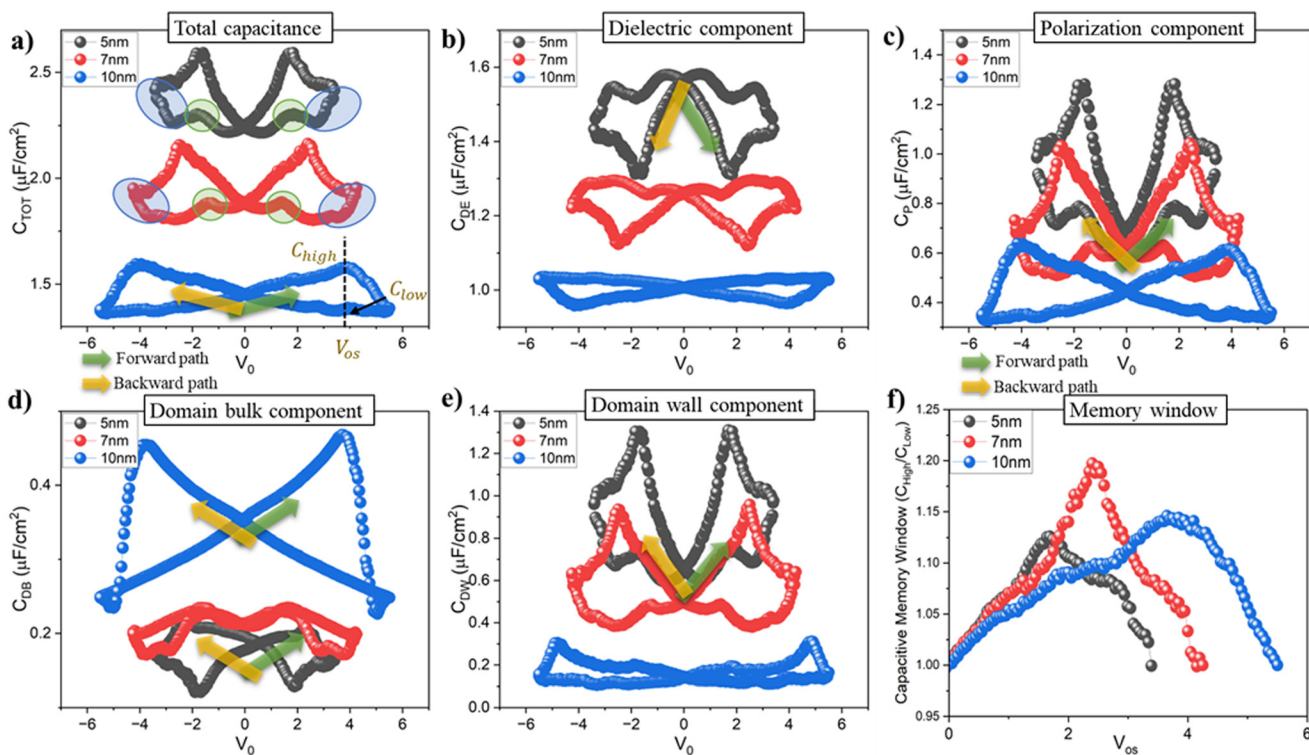


**Fig. 10** (a) Simulated capacitance versus voltage ( $C$ - $V$ ) characteristics of MFIM stack (averaged over 50 samples) across FE thickness of 5, 7, and 10 nm HZO and highlighting the offset voltage ( $V_{os}$ ),  $C_{\text{high}}$  and  $C_{\text{low}}$  used for capacitive memory window calculation. (b) Dielectric capacitance ( $C_{\text{DE}}$ - $V$ ), (c) Polarization capacitance component ( $C_{\text{P}}$ - $V$ ), (d) Domain bulk capacitance ( $C_{\text{DB}}$ - $V$ ) and (e) Domain wall capacitance ( $C_{\text{DW}}$ - $V$ ) of the MFIM stack across different FE thicknesses. (f) Memory window for different offset voltages ( $V_{os}$ ) across FE thicknesses of 5, 7, and 10 nm.

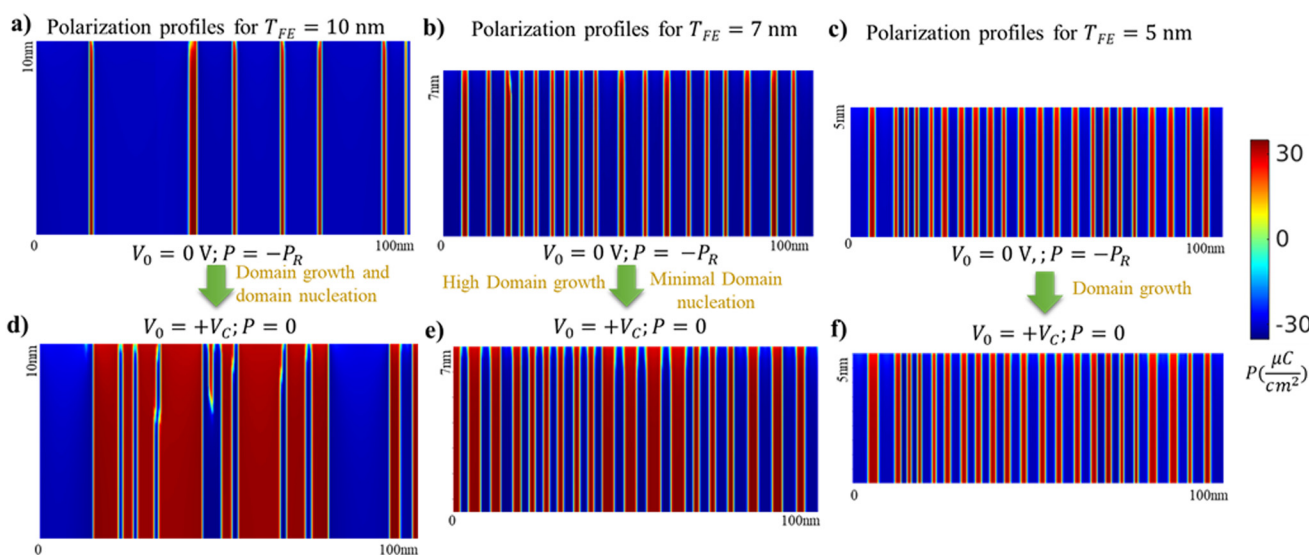


**Fig. 11** Polarization profiles at a bias voltage of 0 V corresponding to negative remanent polarization ( $-P_R$ ) state for FE thicknesses of (a) 10 nm, (b) 7 nm, and (c) 5 nm showing an increase in domain density with scaling the FE thickness. Polarization profiles at bias voltage equal to the coercive voltage of the sample ( $+V_C$ ) corresponding to zero polarization state for FE thicknesses of (d) 10 nm, (e) 7 nm, and (f) 5 nm highlighting the reduced dominance of domain nucleation with FE thickness scaling.

if polarization domain effects were absent, *i.e.*, a lower increase than when the capacitance change is strictly due to thickness scaling as in a dielectric material.

Additionally, we observe an increased range of  $C_{\text{DE}}$  across bias voltages for thinner FE layers (7 and 5 nm), which can be understood as follows. On the forward path, beginning from

the most negative bias voltage, even with the increased domain density, most of the *E*-field is oriented out-of-plane due to the asymmetry in the magnitudes of *+P* and *-P* domains. As  $V_0$  increases, this asymmetry decreases, shifting the *E*-field from out-of-plane to in-plane direction. The higher domain density and, in turn, higher DW area in thinner FE layers promote this op-to-ip transformation more than at 10 nm. As a result,  $C_{DE}$  reduces significantly with  $V_0$  increase for lower FE thicknesses, leading to a higher range of  $C_{DE}$  as FE thickness scales down.

However, at lower FE thicknesses, we observe deviations in the *C-V* characteristics from the traditional butterfly curves<sup>59,60</sup> (highlighted in Fig. 10a). First, there is an initial decrease in capacitance (highlighted in blue in Fig. 10a) as  $V_0$  moves from extreme negative (positive) bias voltage towards zero on the forward (backward) voltage paths. This decrease stems from the wide domain wall response at the FE-DE interface. At high negative  $V_0$ , conical *+P* domains form near the FE-DE interface with the *P-E* position of *+P* domain point at the interface along the high-slope segment of the LK curve (refer to section 6.2.1). As  $V_0$  increases, these regions shift toward the low-slope segment, reducing its response to the sinusoidal waveform. This effect is more pronounced at lower FE thicknesses due to higher DW density, reducing  $C_{TOT}$  as highlighted in blue in Fig. 10a. Some experimental characteristics presented show a capacitance increase at higher voltages<sup>30,31,58</sup> for scaled FE thicknesses, which is often attributed to leakage currents.<sup>58</sup> The prevalence of leakage currents at high voltages makes the identification and validation of the capacitance increase due to the wide DW response challenging.

Additionally, small bumps in the capacitance (highlighted in green in Fig. 10a) are observed as  $V_0$  transitions from most negative (positive) voltage to 0 V. This phenomenon is also due to the wide-DW response at the FE-DE interface. At high negative  $V_0$ , the “softer” DW regions associated with the conical *+P* domains have their *P-E* positions along the moderate-slope segment of the LK curve (refer to section 6.2.1). As  $V_0$  increases, these *P-E* positions shift along the moderate-slope segment towards the high-slope segment, briefly enhancing their response to the sinusoidal waveform. With further increase in  $V_0$ , these *P-E* positions eventually move to the low-slope segment, reducing  $C_{TOT}$ . Due to the higher domain density at lower FE thicknesses, this effect creates the observed bumps in  $C_{TOT}$ . This phenomenon needs further investigation with rigorous 3D simulations and experimental characterizations at scaled FE thickness and device dimensions.

We further explore the impact of increased domain density and FE thickness scaling on the capacitive memory window (MW), a crucial metric for capacitive compute-in-memory (CiM) applications.<sup>17-19</sup> In capacitive CiM applications, FE capacitors are utilized by creating a capacitance difference between the forward and backward paths (or the low and high capacitance states) at zero bias voltage. This difference is achieved either by introducing a non-zero offset voltage ( $V_{os}$ ) across the FE capacitor or by incorporating traps, leading to

asymmetric butterfly *C-V* characteristics.<sup>18</sup> For our analysis, we consider the former method of using offset voltage.

We vary the offset voltage (Fig. 10a) and examine the trends in the capacitive MW, defined as the ratio between the high ( $C_{high}$ ) and low ( $C_{low}$ ) capacitance states<sup>17</sup> (as marked in Fig. 10a). We observe a non-monotonic capacitive MW response to  $V_{os}$  across FE thicknesses (Fig. 10f): the capacitive MW initially increases with  $V_{os}$  and then decreases leading to a peak in the MW at certain  $V_{os}$ , due to the butterfly shape of the FE *C-V* characteristics.

Peak capacitive MW shows a non-monotonic dependence on FE thickness (Fig. 10f). As thickness scales from 10 to 7 nm, capacitive MW peaks increase, largely due to the expanded range of  $C_{TOT}$ . However, scaling to 5 nm reduces the peak capacitive MW, despite the increased  $C_{TOT}$  range. This reduction occurs because the  $C_{high}$  peak at 5 nm coincides with a bump in the  $C_{low}$  branch, reducing the peak  $C_{high}/C_{low}$  ratio. As mentioned, this behavior and the bumps in the butterfly curves warrant further investigation.

Nevertheless, the dependence of capacitive MW on FE thickness highlights the important role played by P-domain configurations on the MFIM capacitance behavior. If the capacitance changes were solely due to geometry (thickness) scaling, the MW would remain constant across different FE thicknesses. However, the change in the capacitive MW with FE thickness underlines the importance of understanding the effects of polarization domain configurations and switching mechanisms to drive application-driven FE capacitance devices.

## 9 Conclusions

In summary, we have investigated the butterfly ferroelectric capacitance–voltage characteristics, emphasizing the contributions of the dielectric and polarization capacitance components and the physical mechanisms governing them. We have identified and examined three key mechanisms governing the polarization capacitance component. First, the domain bulk response, the response of the regions away from the domain walls, contributes significantly to the ferroelectric capacitance at higher FE thicknesses. Second, the wide domain wall response at the FE-DE interface is prevalent only at the extreme negative and positive bias voltages. Third, the domain wall vicinity response near the domain wall regions plays a crucial role as FE thickness scales down. We further discuss the impact of FE thickness scaling and the resultant increase in the domain density on the capacitance–voltage characteristics and the capacitive memory window, showing a non-monotonic trend in the peak capacitive memory window as a function of FE thickness.

## Author contributions

Conceptualization: R.K., A.K.S., M.M.F. and S.K.G.; data curation and formal Analysis: R.K. and S.K.G; funding acquisition:



S.K.G.; investigation: R.K.; methodology: R.K., A.K.S., M.M.F. and S.K.G; project administration: S.K.G.; software: R.K., A.K.S. and S.K.G.; resources: A.K.S. and S.K.G; supervision: M.M.F. and S.K.G.; validation: M.M.F. and S.K.G.; visualization: R.K., M.M.F. and S.K.G.; writing – original draft: R.K., M.M.F. and S.K.G.; writing – review & editing: R.K., M.M.F. and S.K.G.

## Data availability

Data for this article are available in the following folder “small signal capacitance” at [https://purdue0-my.sharepoint.com/:f/g/personal/kodurur\\_purdue\\_edu/EvPvV56EY21Nstr7IlLM7K8BP-unzl6mRkkL8v4vbros3Q?e=cMuTnk](https://purdue0-my.sharepoint.com/:f/g/personal/kodurur_purdue_edu/EvPvV56EY21Nstr7IlLM7K8BP-unzl6mRkkL8v4vbros3Q?e=cMuTnk).

## Conflicts of interest

There are no conflicts of interest to declare.

## Acknowledgements

This work was supported, in part, by the National Science Foundation under Grant No. 2008412, by the Semiconductor Research Corporation (SRC) Global Research Collaboration (GRC) program under LMD task 2959.001, and by the Center for the Co-Design of Cognitive Systems (COCOSYS), one of the seven centers in JUMP 2.0, an SRC program sponsored by DARPA.

## References

- 1 J. F. Scott, *Science*, 2007, **315**, 954–959.
- 2 T. S. Böscke, J. Müller, D. Bräuhaus, U. Schröder and U. Böttger, *Appl. Phys. Lett.*, 2011, **99**, 102903.
- 3 M. Jerry, S. Dutta, A. Kazemi, K. Ni, J. Zhang, P.-Y. Chen, P. Sharma, S. Yu, X. S. Hu, M. Niemier and S. Datta, *J. Phys. D: Appl. Phys.*, 2018, **51**, 434001.
- 4 K. Ni, B. Grisafe, W. Chakraborty, A. K. Saha, S. Dutta, M. Jerry, J. A. Smith, S. Gupta and S. Datta, 2018 IEEE International Electron Devices Meeting (IEDM), 2018, pp. 16.1.1–16.1.4.
- 5 H. Mulaosmanovic, E. Chicca, M. Bertele, T. Mikolajick and S. Slesazeck, *Nanoscale*, 2018, **10**, 21755–21763.
- 6 E. Ko, H. Lee, Y. Goh, S. Jeon and C. Shin, *IEEE J. Electron Devices Soc.*, 2017, **5**, 306–309.
- 7 U. Schroeder, M. H. Park, T. Mikolajick and C. S. Hwang, *Nat. Rev. Mater.*, 2022, **7**, 653–669.
- 8 H.-J. Lee, M. Lee, K. Lee, J. Jo, H. Yang, Y. Kim, S. C. Chae, U. Waghmare and J. H. Lee, *Science*, 2020, **369**, 1343–1347.
- 9 H. Mulaosmanovic, T. Mikolajick and S. Slesazeck, *ACS Appl. Mater. Interfaces*, 2018, **10**, 23997–24002.
- 10 M. Hoffmann, M. Pešić, K. Chatterjee, A. I. Khan, S. Salahuddin, S. Slesazeck, U. Schroeder and T. Mikolajick, *Adv. Funct. Mater.*, 2016, **26**, 8643–8649.
- 11 A. K. Saha, K. Ni, S. Dutta, S. Datta and S. Gupta, *Appl. Phys. Lett.*, 2019, **114**, 202903.
- 12 V. K. Varadan, K. A. Jose, V. V. Varadan, R. Hughes and J. F. Kelly, *Microwave J.*, 1995, **38**, 244–249.
- 13 D. Ghodgaonkar, R. Hughes, F. Selmi, V. Varadan and V. Varadan, IEEE Antennas and Propagation Society International Symposium 1992 Digest, 1992, vol. 1, pp. 272–275.
- 14 Z. Wang and A. I. Khan, *IEEE J. Explor. Solid-State Comput. Devices Circuits*, 2019, **5**, 151–157.
- 15 N. Thakuria, A. K. Saha, S. K. Thirumala, B. Jung and S. K. Gupta, *IEEE Trans. Electron Devices*, 2019, **66**, 2415–2423.
- 16 K. M. Johnson, *J. Appl. Phys.*, 1962, **33**, 2826–2831.
- 17 S. Mukherjee, J. Bizindavyi, S. Clima, M. I. Popovici, X. Piao, K. Katcko, F. Catthoor, S. Yu, V. V. Afanas'ev and J. Van Houdt, *IEEE Electron Device Lett.*, 2023, **44**, 1092–1095.
- 18 T.-H. Kim, O. Phadke, Y.-C. Luo, H. Mulaosmanovic, J. Mueller, S. Duenkel, S. Beyer, A. I. Khan, S. Datta and S. Yu, *IEEE Electron Device Lett.*, 2023, **44**, 1628–1631.
- 19 S. Yu, Y.-C. Luo, T.-H. Kim and O. Phadke, *IEEE Electron Devices Mag.*, 2023, **1**, 23–32.
- 20 M. Narayanan, S. Tong, B. Ma, S. Liu and U. Balachandran, *Appl. Phys. Lett.*, 2012, **100**, 022907.
- 21 H. Li and G. Subramanyam, *IEEE Trans. Ultrason. Ferroelectr. Freq. Control*, 2009, **56**, 1861–1867.
- 22 C. J. Brennan, *Integr. Ferroelectr.*, 1992, **2**, 73–82.
- 23 C. Ang and Z. Yu, *Appl. Phys. Lett.*, 2004, **85**, 3821–3823.
- 24 Q. M. Zhang, H. Wang, N. Kim and L. E. Cross, *J. Appl. Phys.*, 1994, **75**, 454–459.
- 25 R. Placeres-Jiménez, J. P. Rino, A. M. Gonçalves and J. A. Eiras, *J. Phys. D: Appl. Phys.*, 2015, **48**, 465301.
- 26 C. Kittel, *Phys. Rev.*, 1951, **83**, 458–458.
- 27 L. Jin, V. Porokhonskyy and D. Damjanovic, *Appl. Phys. Lett.*, 2010, **96**, 242902.
- 28 Y.-C. Luo, J. Hur, P. Wang, A. I. Khan and S. Yu, *Appl. Phys. Lett.*, 2020, **117**, 073501.
- 29 M. Massarotto, F. Driussi, A. Affanni, S. Lancaster, S. Slesazeck, T. Mikolajick and D. Esseni, *Solid-State Electron.*, 2023, **200**, 108569.
- 30 M. Segatto, M. Massarotto, S. Lancaster, Q. T. Duong, A. Affanni, R. Fontanini, F. Driussi, D. Lizzit, T. Mikolajick, S. Slesazeck and D. Esseni, ESSDERC 2022 – IEEE 52nd European Solid-State Device Research Conference (ESSDERC), 2022, pp. 340–343.
- 31 M. Massarotto, M. Segatto, F. Driussi, A. Affanni, S. Lancaster, S. Slesazeck, T. Mikolajick and D. Esseni, 2023 35th International Conference on Microelectronic Test Structure (ICMTS), 2023, pp. 1–6.
- 32 D. Bolten, U. Böttger and R. Waser, *J. Eur. Ceram. Soc.*, 2004, **24**, 725–732.
- 33 R. Koduru, I. Ahmed, A. K. Saha, X. Lyu, P. Ye and S. K. Gupta, *J. Appl. Phys.*, 2023, **134**, 084104.
- 34 A. K. Saha, M. Si, P. D. Ye and S. K. Gupta, *Appl. Phys. Lett.*, 2021, **119**, 122903.
- 35 C. E. Krill III and L. Q. Chen, *Acta Mater.*, 2002, **50**, 3059–3075.



36 B. J. Rodriguez, Y. H. Chu, R. Ramesh and S. V. Kalinin, *Appl. Phys. Lett.*, 2008, **93**, 142901.

37 S. Mantri, J. Oddershede, D. Damjanovic and J. E. Daniels, *Acta Mater.*, 2017, **128**, 400–405.

38 S. Mantri and J. E. Daniels, *IEEE Trans. Ultrason. Ferroelectr. Freq. Control*, 2018, **65**, 1517–1524.

39 T. K. Paul, A. K. Saha and S. K. Gupta, *Adv. Electron. Mater.*, 2024, **10**, 2300400.

40 K. Park, D. Kim, K. Lee, H.-J. Lee, J. Kim, S. Kang, A. Lin, A. J. Pattison, W. Theis, C. H. Kim, H. Choi, J. W. Cho, P. Ercius, J. H. Lee, S. C. Chae and J. Park, *ACS Nano*, 2024, **18**(38), 26315–26326.

41 S. Zhang, Q. Zhang, F. Meng, T. Lin, B. Zeng, L. Gu, M. Liao and Y. Zhou, *Research*, 2023, **6**, 0093.

42 J. Li, Y. Qu, M. Si, X. Lyu and P. D. Ye, 2020 IEEE Symposium on VLSI Technology, Honolulu, HI, USA, 2020, pp. 1–2.

43 M. H. Park, Y. H. Lee, H. J. Kim, T. Schenk, W. Lee, K. D. Kim, F. P. G. Fengler, T. Mikolajick, U. Schroeder and C. S. Hwang, *Nanoscale*, 2017, **9**, 9973–9986.

44 R. Koduru, A. K. Saha, M. Si, X. Lyu, P. D. Ye and S. K. Gupta, 2021 IEEE International Electron Devices Meeting (IEDM), 2021, pp. 15.2.1–15.2.4.

45 A. K. Saha and S. K. Gupta, *Sci. Rep.*, 2020, **10**, 10207.

46 L. Hong, A. K. Soh, Y. C. Song and L. C. Lim, *Acta Mater.*, 2008, **56**, 2966–2974.

47 J. Müller, T. S. Bösecke, U. Schröder, S. Mueller, D. Bräuhaus, U. Böttger, L. Frey and T. Mikolajick, *Nano Lett.*, 2012, **12**, 4318–4323.

48 S.-C. Chang, K. Chae, M. I. Popovici, C.-C. Lin, S. Siddiqui, I.-C. Tung, J. Bizindavyi, B. G. Alpizar, N. Haratipour, M. Metz, J. Kavalieros, G. S. Kar, A. Kummel, K. Cho and U. E. Avci, 2022 International Electron Devices Meeting (IEDM), 2022, pp. 13.1.1–13.1.4.

49 C. Kittel, *Phys. Rev.*, 1951, **82**, 729–732.

50 A. N. Morozovska, M. V. Strikha, K. P. Kelley, S. V. Kalinin and E. A. Eliseev, *Phys. Rev. Appl.*, 2023, **20**, 054007.

51 T. R. Kim, A. K. Saha and S. K. Gupta, 2023 Device Research Conference (DRC), 2023, pp. 1–2.

52 S. Deng, G. Yin, W. Chakraborty, S. Dutta, S. Datta, X. Li and K. Ni, 2020 IEEE Symposium on VLSI Technology, 2020, pp. 1–2.

53 K. Ni, W. Chakraborty, J. Smith, B. Grisafe and S. Datta, 2019 Symposium on VLSI Technology, 2019, pp. T40–T41.

54 J. P. B. Silva, R. Alcala, U. E. Avci, N. Barrett, L. Bégon-Lours, M. Borg, S. Byun, S.-C. Chang, S.-W. Cheong, D.-H. Choe, J. Coignus, V. Deshpande, A. Dimoulas, C. Dubourdieu, I. Fina, H. Funakubo, L. Grenouillet, A. Gruverman, J. Heo, M. Hoffmann, H. A. Hsain, F.-T. Huang, C. S. Hwang, J. Íñiguez, J. L. Jones, I. V. Karpov, A. Kersch, T. Kwon, S. Lancaster, M. Lederer, Y. Lee, P. D. Lomenzo, L. W. Martin, S. Martin, S. Migita, T. Mikolajick, B. Noheda, M. H. Park, K. M. Rabe, S. Salahuddin, F. Sánchez, K. Seidel, T. Shimizu, T. Shiraishi, S. Slesazeck, A. Toriumi, H. Uchida, B. Vilquin, X. Xu, K. H. Ye and U. Schroeder, *APL Mater.*, 2023, **11**, 089201.

55 M. Pešić, F. P. G. Fengler, L. Larcher, A. Padovani, T. Schenk, E. D. Grimley, X. Sang, J. M. LeBeau, S. Slesazeck, U. Schroeder and T. Mikolajick, *Adv. Funct. Mater.*, 2016, **26**, 4601–4612.

56 W. Yang, J. Pan, Y. Bao, Y. Shao, Y. Wang, Y. Deng, J. Jiang, Q. Yang, X. Zhong and L. Jiang, *Comput. Mater. Sci.*, 2022, **213**, 111607.

57 M. Lee, D. M. Narayan, J.-H. Kim, D. N. Le, S. Shirodkar, S. Park, J. Kang, S. Lee, Y. Ahn, S. W. Ryu, S. J. Kim and J. Kim, *ACS Appl. Electron. Mater.*, 2024, **6**, 5391–5401.

58 M. A. Sahiner, R. J. Vander Valk, J. Steier, J. Savastano, S. Kelty, B. Ravel, J. C. Woicik, Y. Ogawa, K. Schmidt, E. A. Cartier, J. L. Jordan-Sweet, C. Lavoie and M. M. Frank, *Appl. Phys. Lett.*, 2021, **118**, 092903.

59 H.-H. Chen, R.-Y. Liao, W.-C. Chou, H.-H. Hsu, C.-H. Cheng and C.-C. Huang, *IEEE J. Electron Devices Soc.*, 2022, **10**, 947–952.

60 X. Lyu, M. Si, X. Sun, M. A. Capano, H. Wang and P. Ye, 2019 Symposium on VLSI Technology, 2019, pp. T44–T45.

61 A. K. Saha and S. K. Gupta, *J. Appl. Phys.*, 2021, **129**, 080901.

62 A. K. Saha, M. Si, K. Ni, S. Datta, P. D. Ye and S. K. Gupta, 2020 IEEE International Electron Devices Meeting (IEDM), San Francisco, CA, USA, 2020, pp. 4.3.1–4.3.4.

63 E. A. Eliseev, A. N. Morozovska, S. V. Kalinin, Y. Li, J. Shen, M. D. Glinchuk, L.-Q. Chen and V. Gopalan, *J. Appl. Phys.*, 2009, **106**, 084102.

64 H. W. Park, J. Roh, Y. B. Lee and C. S. Hwang, *Adv. Mater.*, 2019, **31**, 1805266.

65 T. K. Paul, A. K. Saha and S. K. Gupta, *Sci. Rep.*, 2024, **14**, 9861.

